

The SNARE Sec22b has a non-fusogenic function in plasma membrane expansion

Maja Petkovic^{1,2,3,4,12}, Aymen Jemaïel^{3,5,11}, Frédéric Daste^{1,2,3,6,11}, Christian G. Specht⁷, Ignacio Izeddin⁸, Daniela Vorkel⁹, Jean-Marc Verbavatz^{3,9}, Xavier Darzacq⁸, Antoine Triller⁷, Karl H. Pfenninger¹⁰, David Tareste^{1,2,3}, Catherine L. Jackson^{3,5,13} and Thierry Galli^{1,2,3,13}

Development of the nervous system requires extensive axonal and dendritic growth during which neurons massively increase their surface area. Here we report that the endoplasmic reticulum (ER)-resident SNARE Sec22b has a conserved non-fusogenic function in plasma membrane expansion. Sec22b is closely apposed to the plasma membrane SNARE syntaxin1. Sec22b forms a *trans*-SNARE complex with syntaxin1 that does not include SNAP23/25/29, and does not mediate fusion. Insertion of a long rigid linker between the SNARE and transmembrane domains of Sec22b extends the distance between the ER and plasma membrane, and impairs neurite growth but not the secretion of VSV-G. In yeast, Sec22 interacts with lipid transfer proteins, and inhibition of Sec22 leads to defects in lipid metabolism at contact sites between the ER and plasma membrane. These results suggest that close apposition of the ER and plasma membrane mediated by Sec22 and plasma membrane syntaxins generates a non-fusogenic SNARE bridge contributing to plasma membrane expansion, probably through non-vesicular lipid transfer.

Plasma membrane (PM) expansion is an essential step in cell growth. In budding yeast, formation of a daughter cell bud precedes cell division and requires a doubling of the PM surface within each cell cycle. Neurons provide one of the most striking examples of cell growth. Their elaborate processes extend up to hundreds of micrometres from the cell body¹, requiring an increase in their PM surface by 20% per day during development². The continuous addition of new membrane components required for this expansion³ is thought to occur by SNARE-mediated fusion of secretory vesicles with the PM (refs 4–7). However, it remains unclear whether additional mechanisms complementary to membrane fusion contribute to neurite growth, such as synthesis and non-vesicular transfer of lipids, which have been shown to localize preferentially at membrane contact sites (MCSs) between the ER and other organelles including the PM (refs 8–10).

SNAREs are transmembrane proteins that are essential for membrane fusion¹¹. SNARE-mediated fusion is a multi-step process whereby a *trans*-SNARE complex, composed of an R-SNARE on one

membrane and three Q-SNAREs on the other, assembles to bridge the two membranes and to bring them into close proximity. This partially assembled SNARE complex then proceeds to full zipping, which further pulls together the lipid bilayers and triggers their fusion^{12,13}. In mammals, hitherto the R-SNAREs Syb2/VAMP2 and TI-VAMP/VAMP7 have been implicated in neuronal growth. TI-VAMP is required for axonal and dendritic growth of neurons in culture^{4,5,14}. A recent study revealed a requirement for VAMP2 in axonal growth⁶. Yet, knockouts of both TI-VAMP (ref. 15) and VAMP2 (refs 16,17) do not have major defects in neurite growth. To evaluate mechanisms of membrane expansion, we began by analysing growth cones for additional R-SNAREs that could participate in growth, and found the R-SNARE Sec22b to be as highly enriched as VAMP2 and TI-VAMP. We found that ER-localized Sec22 interacted with the Q-SNAREs syntaxin1 (Stx1) in neurons and Sso1, its homologue in budding yeast, suggesting conservation of the interaction. Even though Sec22b-positive structures were found closely apposed to PM Stx1, Sec22b and Stx1 were not sufficient to mediate fusion *in vitro*

¹INSERM, U950, F-75013 Paris, France. ²Université Paris Diderot, Sorbonne Paris Cité, ERL U950, F-75013 Paris, France. ³CNRS, UMR 7592, Institut Jacques Monod, F-75013 Paris, France. ⁴Ecole des Neurosciences de Paris (ENP), F-75006 Paris, France. ⁵Membrane Dynamics and Intracellular Trafficking, Institute Jacques Monod, F-75013 Paris, France. ⁶Ecole Doctorale Frontières du Vivant (FdV) – Programme Bettencourt, Université Paris Descartes, Sorbonne Paris Cité, F-75004 Paris, France. ⁷Institut de Biologie de l'École Normale Supérieure (IBENS), Biologie Cellulaire de la Synapse, INSERM U1024, CNRS UMR8197, F-75005 Paris, France. ⁸Institut de Biologie de l'École Normale Supérieure (IBENS), Functional Imaging of Transcription, INSERM U1024, CNRS UMR8197, F-75005 Paris, France. ⁹Max Planck Institute of Molecular Cell Biology and Genetics, 01307 Dresden, Germany. ¹⁰Linda Crnic Institute for Down Syndrome and Department of Pediatrics, University Colorado School of Medicine, Aurora, Colorado 80045, USA. ¹¹These authors contributed equally to this work. ¹²Present address: Howard Hughes Medical Institute, Departments of Physiology, Biochemistry, and Biophysics, University of California, San Francisco, San Francisco, California 94158, USA. ¹³Correspondence should be addressed to C.J. or T.G. (e-mail: jackson@ijm.univ-paris-diderot.fr or thierry.galli@inserm.fr)

or exocytosis *in vivo*, suggesting that they may rather contribute to tethering of the ER to the PM. We found that introduction of a long rigid spacer between the SNARE and the transmembrane domains of Sec22b increased the gap at ER–PM contact sites, and reduced neuronal growth, but not the transport of VSV-G to the cell surface. Knockdown of Sec22b did not impair store-operated calcium entry (SOCE). However, we found that Sec22 and the yeast syntaxin homologue Sso1 interacted with the lipid transfer proteins Osh2 and Osh3. We further demonstrated that the elimination of Sec22 function compromised the phosphatidylinositol-4-phosphate (PtdIns(4)P) levels regulated at PM–ER contact sites in yeast. Thus, we conclude that the Sec22–syntaxin interaction functions at ER–PM contact sites, where it may regulate lipid synthesis and transfer, and that this conserved mechanism contributes to PM expansion.

The R-SNARE Sec22b is present in growth cones where it localizes to the ER

During early neuronal development, growing neurites actively add new membrane at the growth cones^{18,19}. Hence, we performed subcellular fractionation of growth cone membranes from newborn mouse brains (Fig. 1a) to establish a repertoire of R-SNAREs that could play a role in neurite growth. We found that the R-SNARE Sec22b was enriched in growth cone membranes to a similar level as VAMP2 and TI-VAMP/VAMP7 (Fig. 1b,c), two R-SNAREs previously implicated in neurite growth^{4–6}. Accordingly, immunocytochemistry in neuronal cultures showed that endogenous Sec22b is localized in the soma and neurites and enriched in growth cones (Fig. 1d), unlike the R-SNAREs Ykt6 and VAMP4 (Supplementary Fig. 1a). Sec22b was shown to localize to the ER and ER–Golgi intermediate compartment (ERGIC), and functions in ER–Golgi anterograde and retrograde transport²⁰. In neurites and growth cones, Sec22b co-localized with the ER, but not with an ERGIC marker (Fig. 1e). Confocal light microscopy and super-resolution microscopy (PALM) further confirmed the ER tubulo-reticular morphology of the Sec22b compartment (Fig. 1f), and live-cell imaging showed that Sec22b has a dynamic reticular pattern in neurites and growth cones characteristic of the ER, entering even thin filopodia (Fig. 1g and Supplementary Videos 1–3). We cannot exclude the possibility that a minor pool of Sec22b in neurites and growth cones is localized to vesicular structures, but we were unable to detect such a pool with the approaches that could robustly detect TI-VAMP and VAMP2 vesicles in neurites^{6,14,21,22}.

Impairment of Sec22b inhibits axonal and dendritic growth

Next, we investigated whether Sec22b is required for neurite growth. To this end we used multiple approaches, namely dominant-negative, short interfering RNA (siRNA) and short hairpin RNA (shRNA) knockdown in culture and *in vivo*. Sec22b contains an amino-terminal regulatory longin domain²³. Longin domains were shown to exert a dominant-negative effect on membrane fusion²⁴ by folding against the SNARE domain²⁵. We found that the expression of the Sec22b longin domain reduced outgrowth of dendrites and axons (Fig. 2a). Next, we confirmed the efficiency of Sec22b siRNA knockdown in mouse cell line L929 with two different siRNAs (Fig. 2b) and we further used siRNA1 that targets the 3' UTR. Cortical neurons were co-transfected with GFP, and siRNA1 or scrambled control at day *in vitro* (DIV)1, and fixed after 48 h of expression. Quantitative analysis revealed that

both axonal and dendritic growth was strongly impaired by Sec22b siRNA knockdown (Fig. 2c). The observed effect was due to Sec22b knockdown, as co-expression of GFP–Sec22b with Sec22b siRNA1 rescued the neurite growth phenotype (Fig. 2c). To further address the function of Sec22b in neuronal growth *in vivo*, we turned to *in utero* electroporation. We used two different previously validated shRNA constructs²⁶. Mouse cortical progenitors were co-electroporated with GFP, and shRNA or scrambled construct as control, at embryonic day (E)14.5 and allowed to develop until E17.5 (Fig. 2d). We found no significant difference between Sec22b knockdown and control condition in neuronal migration (Supplementary Fig. 1b). However, we found a significant reduction in neurite length after 72 h of knockdown with both shRNA1 and shRNA2 compared with control neurons (Fig. 2e). Together, these experiments demonstrate that Sec22b is required for neurite growth both in cultured neurons and *in vivo*.

Sec22b interacts with PM Q-SNARE Stx1

To uncover its function at the molecular level, we next searched for partners of Sec22b by yeast two-hybrid screening of a human fetal brain library. Besides obtaining syntaxin5 (Stx5), the known Sec22b Q-SNARE partner in the early secretory pathway²⁷, we found a direct interaction of Sec22b with the PM Q-SNARE Stx1, in a region containing its SNARE domain (Fig. 3a). Interestingly, no other Q-SNAREs were identified, including SNAP-25, which was found as a partner of TI-VAMP using the same approach and the same library²⁸. To address the interaction of Sec22b with PM Q-SNAREs in neurons, we performed immunoprecipitation of endogenous proteins from both embryonic and adult mouse brains. Sec22b co-immunoprecipitated with Stx1 in both cases (Fig. 3b), but we could not detect Sec22b co-immunoprecipitation with any of the growth cone-localized SNAPs (23, 25, and 29; Fig. 3c), whereas VAMP2 and Stx1 were readily co-immunoprecipitated with SNAP-25, SNAP-23 and SNAP-29 as expected^{17,29} (Fig. 3d–f).

Sec22b does not mediate exocytosis

To gain further insight into Sec22b/Stx1 complex fusion activity, we reconstituted the purified mammalian proteins into liposomes (Supplementary Fig. 2a) and performed liposome fusion assays. ER-like liposomes bearing Sec22b underwent robust fusion with PM-like liposomes containing Stx1/SNAP-25, but no fusion was observed with liposomes containing only Stx1. The lack of fusion was not due to auto-inhibition of Stx1 because we used a Δ Habc activated Stx1 in all experiments and re-addition of soluble SNAP-25 restored fusion efficiency (Fig. 3g,h). As we did not find Sec22b in SNAP23/25/29 immunoprecipitations from either embryonic or adult brains, we conclude that the Sec22b/Stx1 complex is not fusogenic owing to the absence of a PM Q-SNARE light chain. Interestingly, Stx1 clusters have been shown to only partially overlap with SNAP25 at the PM (ref. 30), suggesting the existence of functionally distinct Stx1 clusters.

We next investigated whether Sec22b mediates fusion with the PM *in vivo* using surface staining. As Sec22b does not have an extracellular domain, we carboxy-terminally tagged Sec22b, so that if the Sec22b compartment fused with the PM, it would be detected by extracellularly added anti-GFP antibody. N-terminally

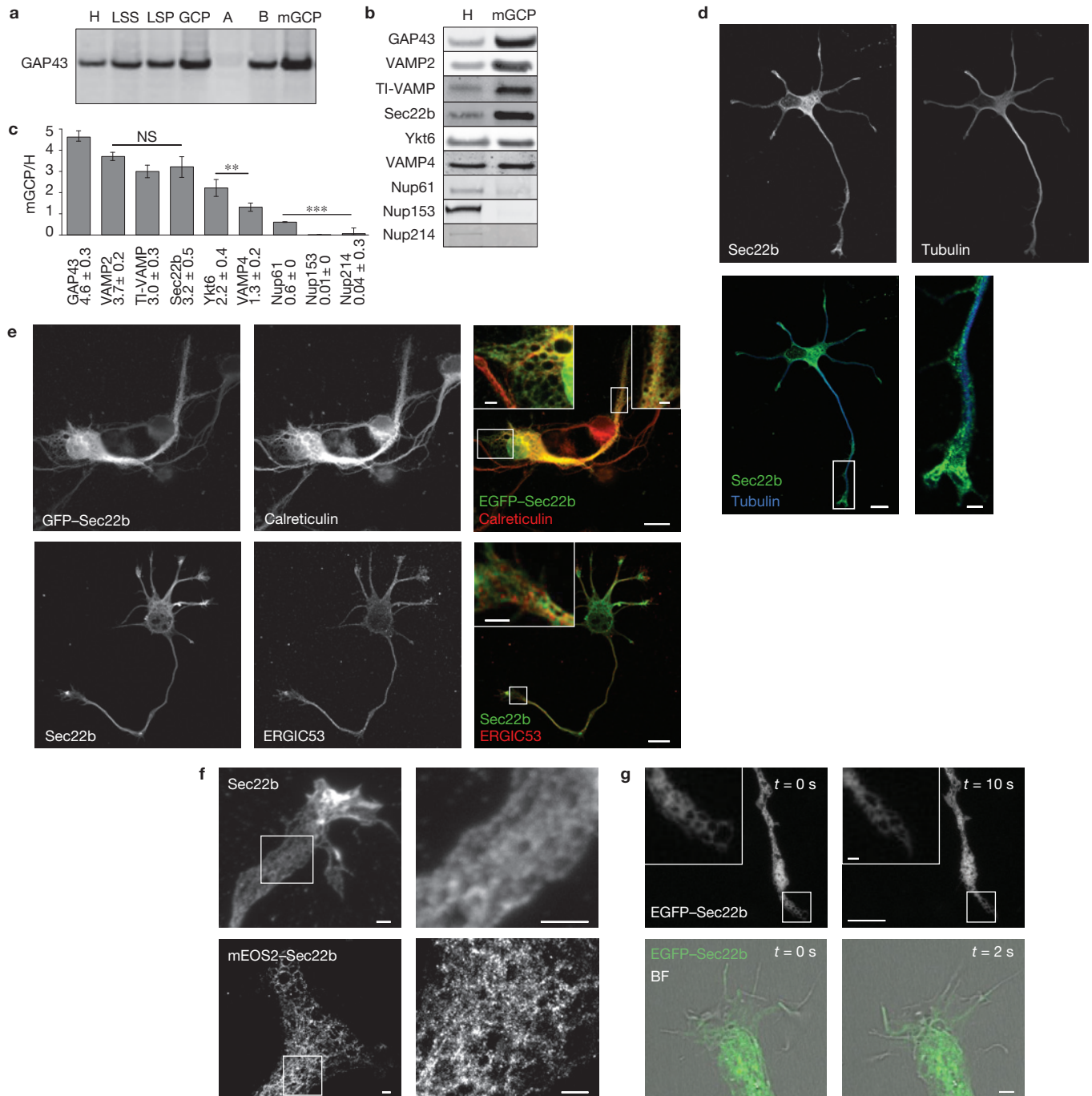


Figure 1 The R-SNARE Sec22b is present in neurites and growth cones where it localizes to the ER. **(a)** Evaluation of successful growth cone membrane subcellular fractionation was performed by loading equal amounts of total proteins of each collected fraction of mouse newborn brains on a gel, and visualization by western blotting for GAP43, a marker of axonal growth cones. H, total brain homogenate; LSP, low-speed pellet; LSS, low-speed supernatant, the parent fraction of GCPs; GCP, resealed growth cone particles; A, fraction containing soluble proteins of H; B, pellet after gradient centrifugation; mGCP, growth cone membranes. **(b)** Representative western blots of R-SNAREs (with GAP43 as a positive control and nucleoporins as a negative control) showing enrichment in mGCP versus H fractions. **(c)** Quantification of enrichment in mGCP versus H, mean \pm s.e.m. ($n=3$ independent growth cone membrane fractionations, 2 independent western blots per fractionation). One-way analysis of variance (ANOVA) $P < 0.0001$,

post-test Bonferroni-corrected t -test is labelled on graph with pairwise comparison with GAP43. $**P < 0.005$, $***P < 0.0005$. **(d)** Endogenous Sec22b is localized in perikaryon, neurites and growth cones. Scale bars: 10 μm , inset: 2 μm . **(e)** Sec22b in neurites and growth cones co-localizes with calreticulin (first row), and is apposed to ERGIC53 (second row). Scale bars: 10 μm , insets: 2 μm . **(f)** 3D reconstruction of confocal z-stack (first row, scale bars: 2 μm) and PALM super-resolution imaging (second row, pixel size: 10 nm, scale bars: 1 μm) show a tubulo-reticular network of endogenous and tagged Sec22b, respectively. **(g)** Live imaging of EGFP-Sec22b in cortical neurons reveals the dynamics of the labelled tubulo-reticular network in neurites (first row, scale bars: 10 μm , inset: 2 μm ; Supplementary Video 2), which enters into thin filopodia of growth cones (second row, scale bars: 2 μm ; Supplementary Video 3). BF, bright field. Uncropped images of blots are shown in Supplementary Fig. 4.

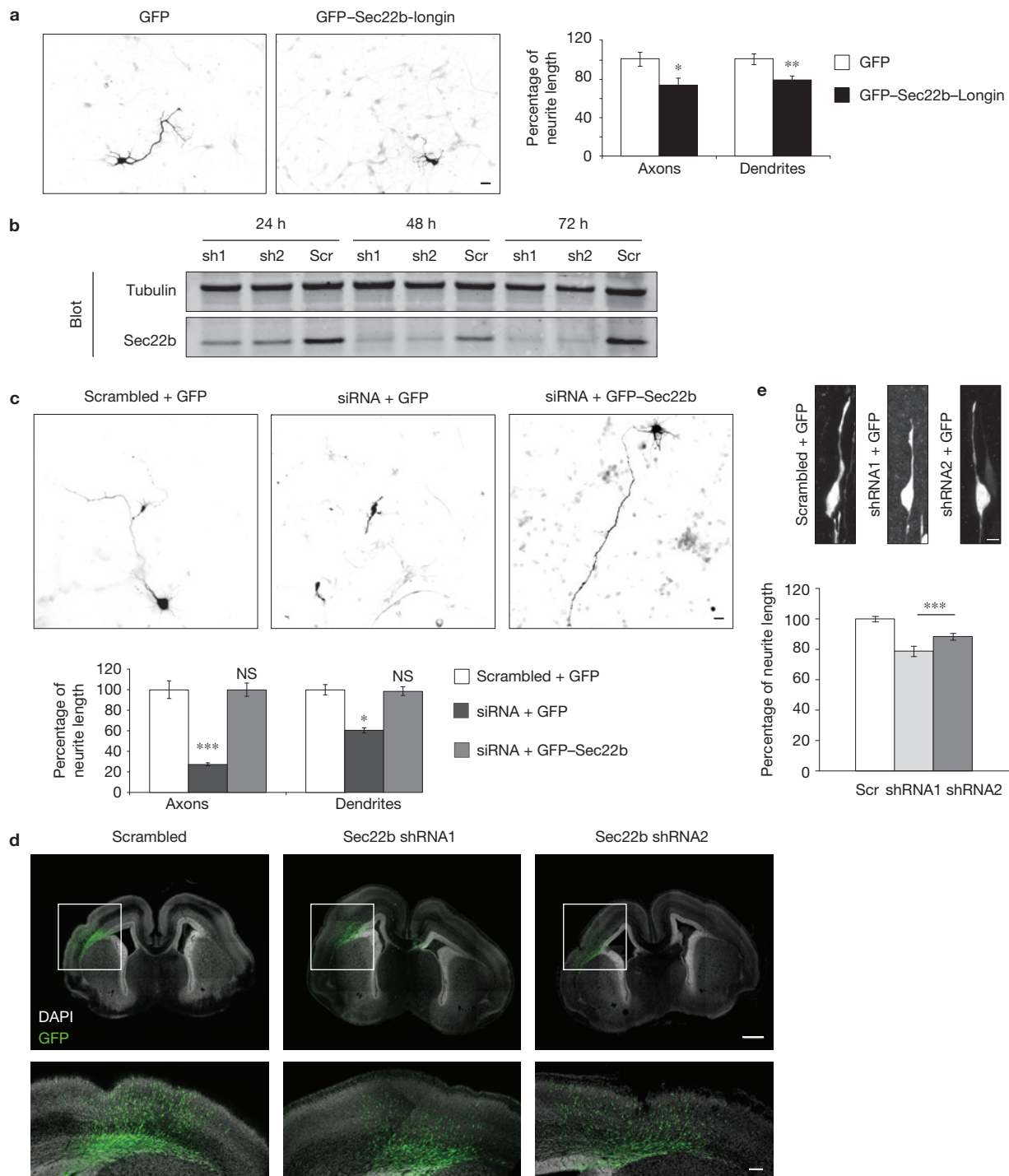


Figure 2 Impairment of Sec22b inhibits neurite growth. **(a)** Dominant-negative mutant of Sec22b impairs axonal (GFP: $n = 96$, GFP-Sec22b-longin: $n = 93$; 3 independent experiments) and dendritic (GFP: $n = 152$, GFP-Sec22b-longin: $n = 155$; 3 independent experiments) growth after 24 h of expression. Student's t -test: $*P < 0.05$, $**P < 0.005$. Graph shows mean \pm s.e.m. Scale bar: 10 μ m. **(b)** Efficiency of siRNA knockdown of Sec22b in mouse cell line L929. **(c)** 48 h of Sec22b siRNA1 knockdown in mouse cortical neurons reduced axonal length (scrambled: $n = 75$, shRNA1: $n = 114$; 3 independent experiments) by $72.9 \pm 5.1\%$, and dendritic length (scrambled: $n = 162$, shRNA1: $n = 242$; 3 independent experiments) by $39.5 \pm 3.4\%$ compared with control neurons. Co-expression of Sec22b siRNA1 with GFP-Sec22b rescued the neurite growth phenotype (axons:

$n = 107$, dendrites: $n = 246$; 3 independent experiments). Scale bar: 10 μ m. Student's t -test: $*P < 0.05$, $***P < 0.0005$. NS, not significant. Graph shows mean \pm s.e.m. **(d)** Sec22b shRNA knockdown with *in utero* electroporation. Scale bars: 500 μ m, inset: 100 μ m. **(e)** Length of the leading process of neurons in cortical plate after 48 h of Sec22b knockdown (scale bar: 10 μ m) was reduced by $21.2 \pm 1.4\%$ with shRNA1 and $11.5 \pm 0.3\%$ with shRNA2 compared with control neurons (scrambled: $n = 3$ embryos, 190 GFP-expressing cells; shRNA1 $n = 2$ embryos, 107 GFP-expressing cells; shRNA2 $n = 3$ embryos, 208 GFP-expressing cells; 2 independent surgeries). One-way ANOVA $***P < 0.0001$, Dunnett's multiple comparison post-test labelled on graph. Graph shows mean \pm s.e.m. Uncropped images of blots are shown in Supplementary Fig. 4.

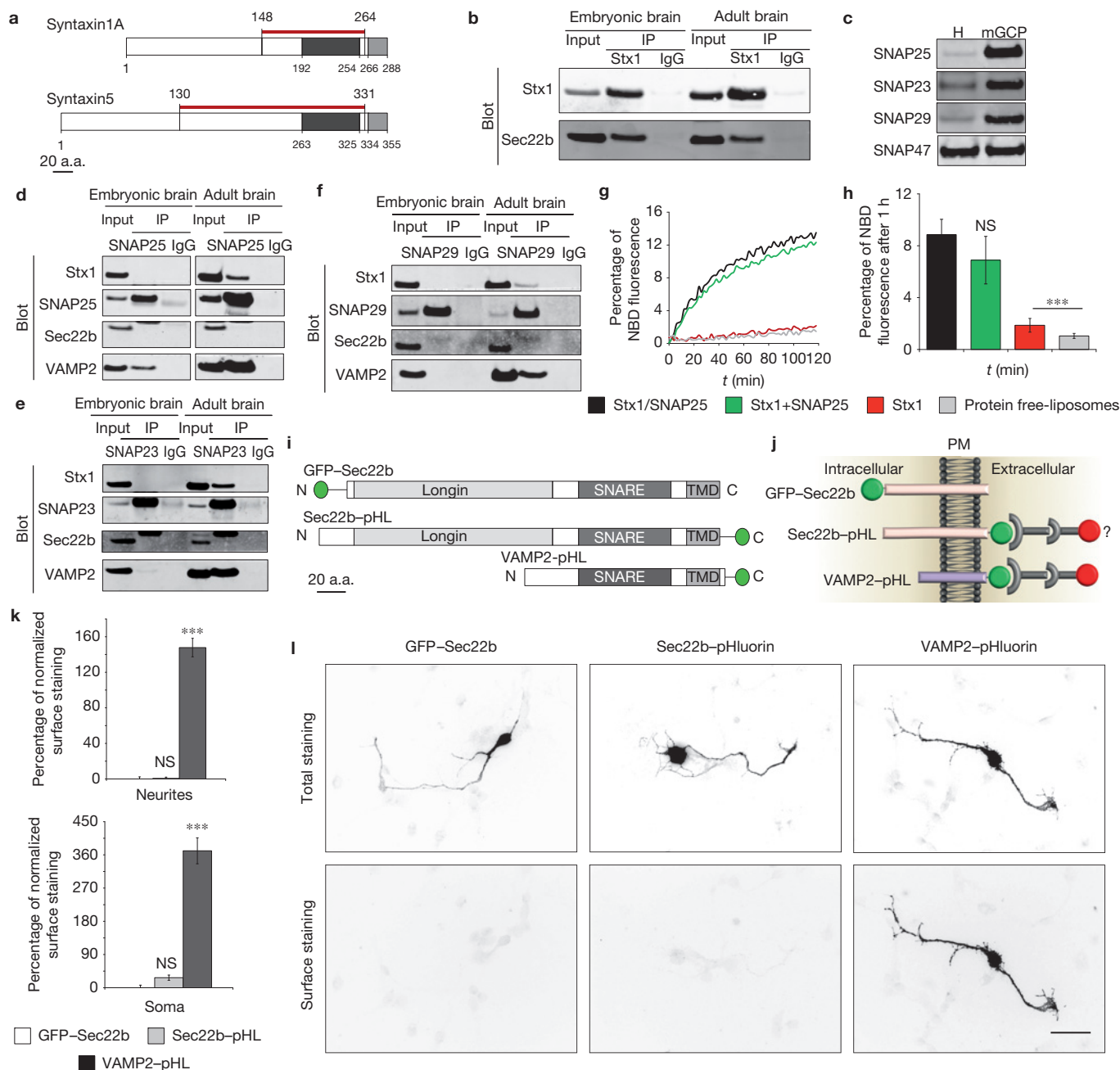


Figure 3 Sec22b interacts with PM Q-SNARE Stx1, but does not mediate exocytosis. **(a)** Stx1 and Stx5 were identified as partners of Sec22b in a yeast two-hybrid screen in a human fetal brain cDNA library. The identified fragments are represented by red lines. **(b)** Stx1 co-immunoprecipitates Sec22b from mouse embryonic and adult brains. **(c)** Growth cone membrane purification from newborn mouse brains. Representative blots of relative enrichment of SNAPs in the growth cone membrane fraction versus total brain homogenate. **(d-f)** SNAP25/23/29 immunoprecipitates Stx1 and VAMP2 as expected, but not Sec22b. Membranes were cut after transfer to allow for independent blotting of Stx1, Sec22b and VAMP2. A scan showing the reassembled membrane is provided in Supplementary Fig. 4. **(g)** Fusion reaction between Sec22b liposomes and Q-SNARE liposomes. Black: co-expressed Stx1/SNAP25; green: separately expressed Stx1 and SNAP25 formed following incubation of Stx1 liposomes with SNAP25; red: Stx1 alone; grey: protein-free liposomes. **(h)** Extent of lipid mixing measured as the NBD fluorescence intensity 60 min after initiation of the reaction

showing mean \pm s.d., $n = 10$ fusion reactions per condition (4 independent liposome preparations, 2–3 independent fusion reactions per preparation). One-way ANOVA $P < 0.0001$, post-test Bonferroni-corrected t -test is labelled on graph with pairwise comparison with Stx1/SNAP25. $P \geq 0.05$ NS, not significant, $***P < 0.0005$. **(i)** A schematic of GFP-Sec22b, Sec22b-pHLuorin (pHL) and VAMP2-pHL. **(j)** Topology of constructs in the PM if fusion is assumed to occur. **(k, l)** Surface staining on neurons transfected with GFP-Sec22b, Sec22b-pHL or VAMP2-pHL. **(k)** Quantitative analysis of surface staining of neurites (GFP-Sec22b: $n = 131$ expressing neurons, Sec22b-pHL: $n = 144$, VAMP2-pHL: $n = 107$, 4 independent experiments) or soma (GFP-Sec22b: $n = 64$ expressing neurons, Sec22b-pHL: $n = 53$, VAMP2-pHL: $n = 74$; 4 independent experiments) versus total staining expressed as normalized ratio to GFP-Sec22b. One-way ANOVA $***P < 0.0001$, Dunnett's multiple comparison post-test labelled on graph. NS, not significant. Graph shows mean \pm s.e.m. **(l)** Representative images. Scale bar: 10 μ m. Uncropped images of blots are shown in Supplementary Fig. 4.

tagged Sec22b was used as a negative control (Fig. 3i,j). In contrast to the strong positive signal observed for VAMP2, we found no detectable Sec22b at the PM (Fig. 3k,l), consistent with previous experimental evidence arguing against fusion of the ER with the PM (ref. 31). Together, these results support the conclusion that the Sec22b/Stx1 complex does not promote fusion of the ER with the PM.

Sec22b comes in close proximity to PM Stx1

We next investigated how closely Sec22b is juxtaposed to PM Stx1. We performed two-dimensional (2D) dual-colour STORM/PALM super-resolution microscopy³² on cortical neurons co-transfected with Stx1-pHluorin and mEOS2-Sec22b (Fig. 4a). We observed overlapping single-molecule punctae of Sec22b and surface staining detected PM Stx1, both in neurites and particularly in growth cones (Fig. 4b). The distance between the closest overlapping fluorophores was measured in two dimensions to be 26 ± 3 nm. To better assess the minimal proximity of Sec22b to surface Stx1, we turned to 3D STORM/PALM super-resolution microscopy^{32,33} (Fig. 4c). Our 3D measurements confirmed the previous 2D data when expressed as projected 2D distance (30 ± 4 nm, Fig. 4d), and allowed us to measure the Euclidean 3D distance ($d_1 = 62 \pm 9$ nm; Fig. 4a,e), where the analysis was done using the x , y and z coordinates of the centre of mass of the fluorophore detections. To measure the minimal distance between the two structures, we included only Sec22b and Stx1 detections that were within 100 nm (in 2D) or 250 nm (in 3D) in this analysis. As additional evidence for the close proximity between the Sec22b and PM Stx1, we performed 3D super-resolution imaging with Sec22b tagged in the opposite orientation with the photoconvertible tag Dendra2 (Sec22b-Dendra2), which is expected to result in a longer distance (Fig. 4a). This was indeed the case, as both projected 2D ($d_1 = 34 \pm 3$ nm; Fig. 4d) and 3D ($d_2 = 78 \pm 23$ nm; Fig. 4a,e) distances between the two fluorophores showed a tendency towards higher values (Fig. 4d,e). Given the location of the tags and the size of antibodies (primary and secondary), the measured distance between Sec22b and surface Stx1 is compatible with the ~ 8 nm membrane distance at which SNARE proteins interact³⁴. We conclude that ER Sec22b, through its interaction with PM Stx1, brings the ER into close proximity with the PM, without mediating their fusion.

Elongating Sec22b increases the distance between the ER and PM, and impairs neurite growth

Next, we investigated whether altering the length of the Sec22b protein affects the distance between the ER and PM. To this end, we generated mutants of Sec22b with polyproline linkers inserted between the SNARE and the transmembrane domain of Sec22b (Fig. 4f). Polyproline stretches form rigid helices, where the number of proline residues determines the length of the helix³⁵. We constructed polyproline linkers of increasing length: 10, 20 and 33 prolines, which correspond to maximum predicted helix lengths of 5.5, 8.6 and 12.6 nm, respectively. The 33-proline insertion mutant is thus predicted to double the distance between the membranes bridged through the Sec22b-Stx1 *trans*-complex if the linker is fully extended and positioned perpendicularly to the ER membrane (Fig. 4g). We used electron tomography to measure the distance between the ER

and PM at contact sites in HeLa cells expressing either wild-type Sec22b or the Sec22b-P33 mutant (Fig. 4h,i). The insertion of 33 prolines in Sec22b resulted in a significant increase of ~ 6 nm in the space separating the ER and PM at contact sites (Fig. 4i). We verified that Sec22b-P33 localization was unchanged (Supplementary Fig. 2b), and that this mutant could still interact with Stx1 (Supplementary Fig. 2c). Next, we expressed our polyproline mutants in cortical neurons. We observed that Sec22b-P33 markedly impaired neurite growth, whereas Sec22b mutants containing shorter polyproline linkers (10 and 20 prolines) had no significant effect on either axonal or dendritic growth (Fig. 4j,k), demonstrating that close distance between ER and PM mediated by Sec22b is required for neurite growth. To exclude the possibility that this was due to impaired secretory pathway function, we used the retention using selective hooks (RUSH) assay³⁶. We found that Sec22b-P33 had no significant effect on the trafficking of VSV-G to the cell surface (Supplementary Fig. 2d,e), suggesting that endogenous Sec22b is able to mediate ER to Golgi transport in the presence of this mutant, and supporting the conclusion that Sec22b has an additional function at ER-PM MCSs independent of its established role in the early secretory pathway.

Sec22b is not required for SOCE

ER-PM contact sites have been shown to be functionally critical for lipid synthesis and non-vesicular lipid traffic⁸⁻¹⁰, as well as SOCE (refs 37,38). Hence, we next investigated whether Sec22b was involved in SOCE. We performed siRNA knockdown of Sec22b in HeLa cells co-transfected with the ER-localized fluorescence resonance energy transfer (FRET)-based ratiometric Ca^{2+} -sensor D1ER (ref. 39). To induce SOCE we depleted the cells of extracellular calcium and measured ER luminal calcium following calcium reintroduction (Fig. 5a, right). Unlike STIM1, Ora1 and α -SNAP (ref. 40), previously shown to be required for SOCE, we did not observe any impairment of SOCE response between the siRNA knockdown and control conditions, indicating that Sec22b, similarly to E-Syts (ref. 41), is not required for SOCE (Fig. 5a, left). As the ER and PM are very closely apposed at MCSs involved in SOCE, we investigated whether we could use SOCE response to further confirm that Sec22b-P33 is increasing the ER-PM distance through a dominant-negative effect. To this end, HeLa cells were transfected with mCherry-Sec22b-P33, and mCherry-tagged wild-type Sec22b or mCherry alone as controls. Luminal ER calcium levels were measured with D1ER (Fig. 5b, right), and cytosolic calcium with Fura2 (Fig. 5c, right). We found that expression of mCherry-Sec22b-P33, but not mCherry-Sec22b nor mCherry alone, lowered luminal ER calcium levels (Fig. 5b, left). In addition, expression of Sec22b-P33 delayed calcium entry into the ER following re-addition of extracellular calcium, as shown by the slope of the FRET increase (see fitting, Fig. 5b, right). To exclude the possibility that this may be due to a defect in calcium entry into the cytosol we measured cytosolic calcium during SOCE. We found that cytosolic calcium levels were slightly increased, as expected when ER levels are reduced, but we found no effect on cytosolic calcium changes following SOCE activation (Fig. 5c, left). Hence, the observed impairments with Sec22b-P33 seem to be a likely consequence of the increased distance between ER and PM at contact sites in cells expressing Sec22b-P33.

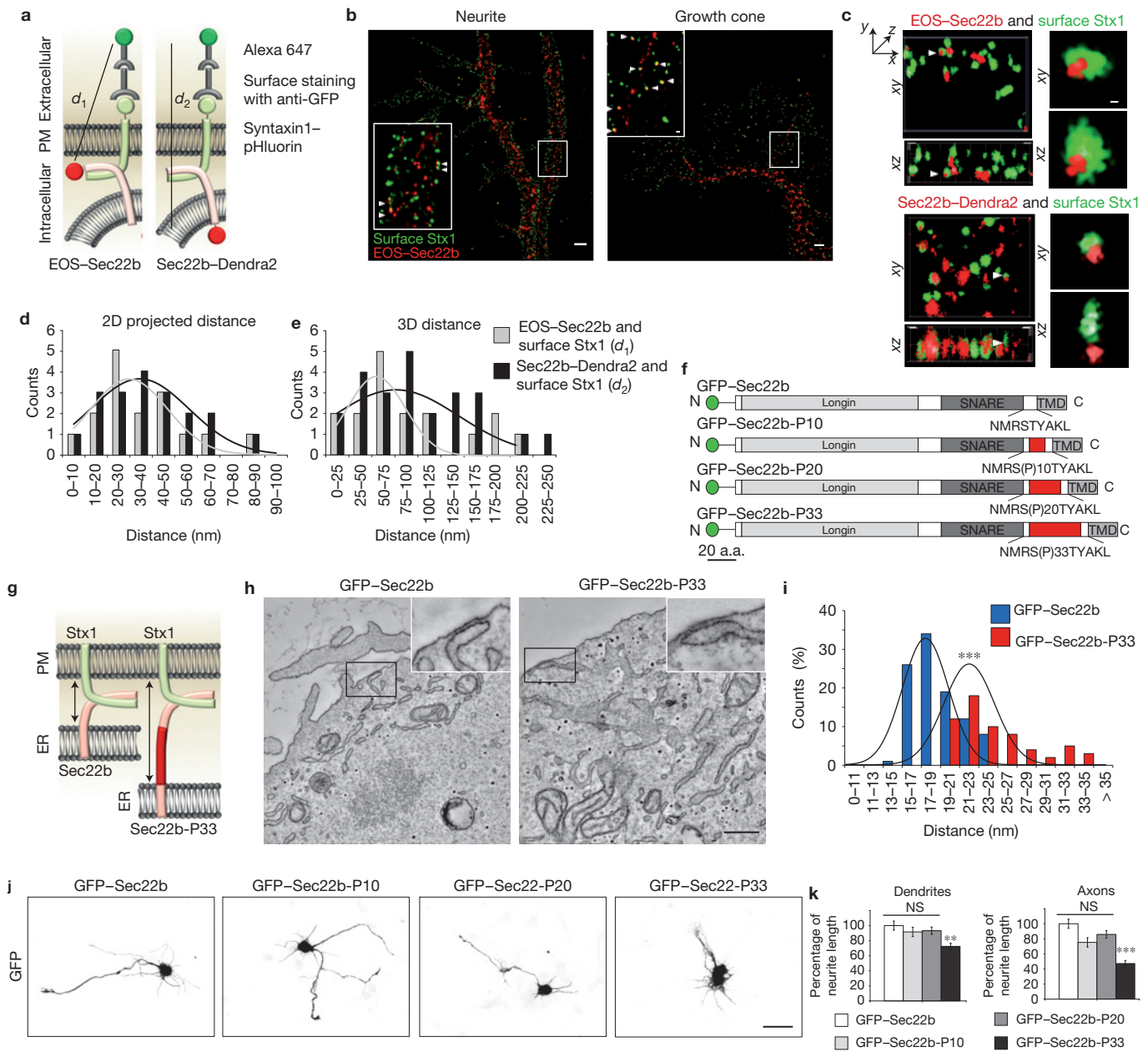


Figure 4 Sec22b comes in close proximity to PM Stx1, and elongating Sec22b increases the distance between the ER and PM, and impairs neurite growth. **(a)** A Schematic of the dual-color STORM/PALM super-resolution experiments. **(b)** 2D dual-color STORM/PALM imaging shows single molecules of surface Stx1 delineating single molecules of EOS-Sec22b with overlapping punctae at a 2D distance 26 ± 3 nm ($n=4$ cells, 3 independent experiments). Scale bars: 1 μ m, inset: 100 nm. **(c)** 3D STORM/PALM acquisition represented as xy and xz projections of surface Stx1-pHluorin and EOS-Sec22b ($n=4$ cells, 2 independent experiments) or Sec22b-Dendra2 ($n=4$ cells, 2 independent experiments). Grid scale: 250 nm, scale bars in insets: 25 nm. The 3D data were quantified both as 2D projections **(d)** as well as 3D spatial representations **(e)**. **(d)** Distribution histogram of 2D projected distance of overlapping punctae measured for EOS-Sec22b and surface Stx1 to be 30 ± 4 nm, and Sec22b-Dendra2 and surface Stx1 34 ± 3 nm. The Kolmogorov-Smirnov test did not reveal a significant difference between Sec22b-Dendra2 and EOS-Sec22b in the acquired sample. $P \geq 0.05$. **(e)** Distribution histogram of Euclidean 3D distance of overlapping punctae determined to be $d_1 = 62 \pm 9$ nm for EOS-Sec22b and surface Stx1 and $d_2 = 78 \pm 23$ nm for Sec22b-Dendra2 and

surface Stx1. The Kolmogorov-Smirnov test did not reveal a significant difference between Sec22b-Dendra2 and EOS-Sec22b in the acquired sample. $P \geq 0.05$. **(f)** A schematic of Sec22b proline mutants. **(g)** Predicted effect of the Sec22b proline insertion on the ER-PM distance. **(h)** Electron tomography slices of HeLa cells transfected with GFP-Sec22b and GFP-Sec22b-P33. Scale bar: 500 nm; insets are threefold higher magnification. **(i)** Distribution histogram of electron microscopy measurements showing a shift towards larger spacing in the GFP-Sec22b-P33 compared with the control, generated on 9 cells, 20 tomograms and 2,000–3,000 images per condition. Quantification is based on $n=100$ ER-PM MCSs for GFP-Sec22b-expressing cells, $n=64$ ER-PM MCSs for GFP-Sec22b-P33. The Kolmogorov-Smirnov test, $***P < 0.001$. **(j)** Representative images of the effect of Sec22b proline linker mutants on neurite growth. Scale bar: 10 μ m. **(k)** Quantification of dendritic and axonal length ($n=136$ for GFP-Sec22b-expressing cells; $n=161$ for GFP-Sec22b-P10; $n=156$ for GFP-Sec22b-P20; $n=88$ for GFP-Sec22b-P33-expressing cells). One-way ANOVA $***P < 0.0001$, Dunnett's multiple comparison post-test labelled on graph. $***P < 0.0001$, $**P < 0.001$. NS, not significant. Graphs show mean \pm s.e.m.

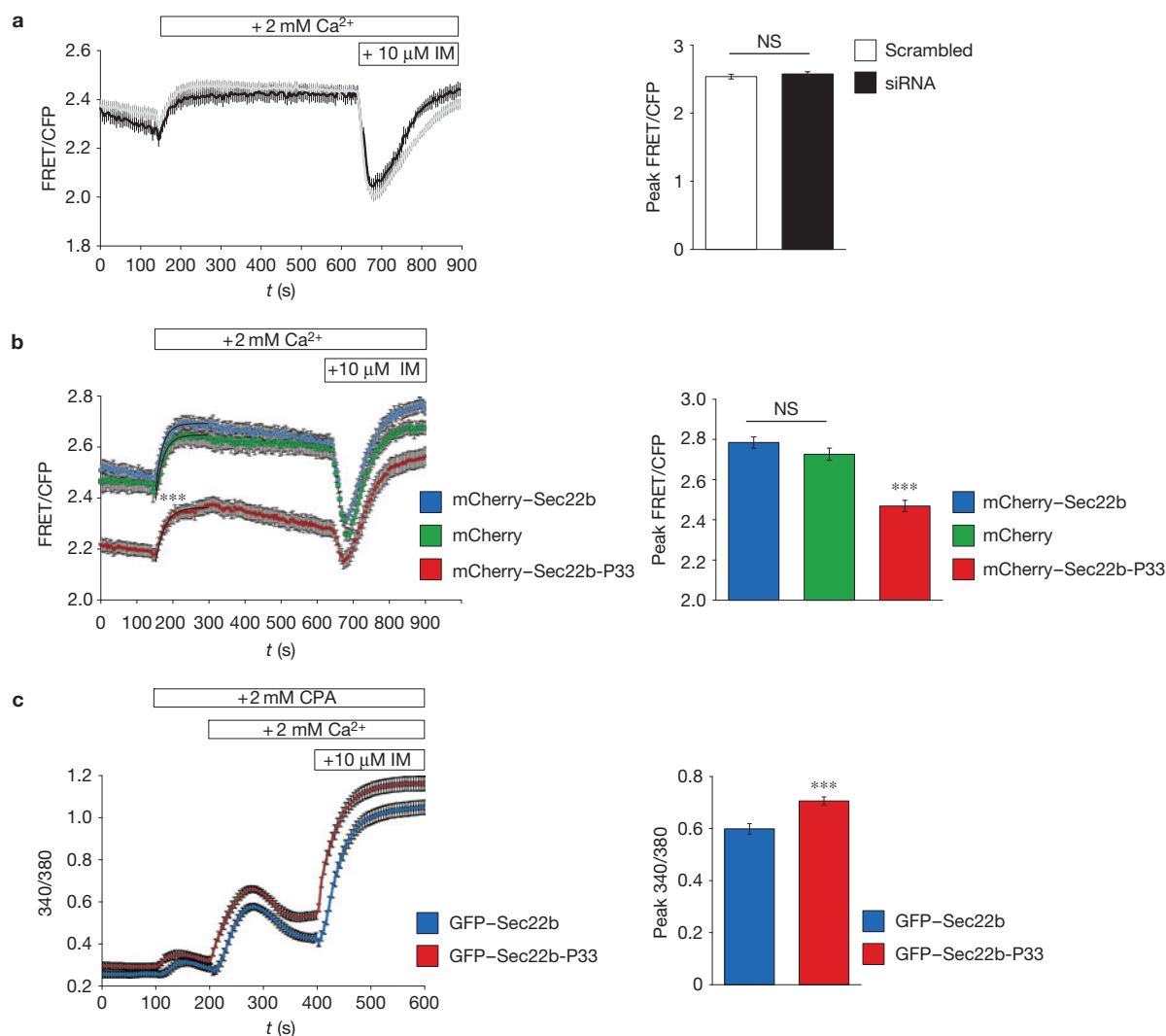


Figure 5 Sec22b is not required for SOCE, but overexpression of elongated Sec22b mutant impairs SOCE. **(a)** HeLa cells were co-transfected with D1ER, an ER-localized FRET-based ratiometric Ca sensor and siRNA or scrambled as a control. Cells were depleted of extracellular calcium for 30 min, followed by time-lapse imaging. Images were acquired every 5 s for 180 frames. Calcium at a final concentration of 2 mM was added at 150 s. Ionomycin (IM) at a final concentration of 10 μ M was added at 640 s. Left: SOCE (150–640 s time interval) peak values presented as mean \pm s.e.m.; $n = 41$ (scrambled) and $n = 41$ (siRNA); Student's t -test: $P \geq 0.05$ NS, non-significant. **(b)** HeLa cells were co-transfected with D1ER and either mCherry, mCherry-Sec22b or mCherry-Sec22b-P33. The calcium imaging protocol was performed as mentioned in **a**. The observed difference in slope following calcium addition of mCherry-Sec22b-P33 compared with controls was quantified by fitting with a single exponential ($f(x) = a + (b - a) * (1 - \exp(-c * x))$); rate c (mCherry) = 2.614 ± 0.003397 , c (mCherry-Sec22b) = 2.664 ± 0.003051 , c (mCherry-Sec22b-P33) = 2.326 ± 0.003428 , best-fit

value \pm s.e.m.), and nonlinear regression analysis revealed a statistically significant difference ($***P < 0.0001$) between the mCherry-Sec22b-P33 and mCherry or mCherry-Sec22b. Left: SOCE (150–640 s time interval) peak values presented as mean \pm s.e.m.; $n = 60$ mCherry-Sec22b-expressing cells, $n = 78$ mCherry and $n = 63$ mCherry-Sec22b-P33-expressing cells from 5 independent experiments; Student's t -test: $P \geq 0.05$ NS, not significant; $***P < 0.0005$. **(c)** HeLa cells transfected with GFP-Sec22b or GFP-Sec22b-P33 were loaded with Fura2, depleted of extracellular calcium and time-lapse imaged with 5 s intervals. CPA at a final concentration of 20 μ M was added at 100 s, calcium at a final concentration of 2 mM at 200 s, and ionomycin (IM) at a final concentration of 10 μ M at 400 s. GFP-Sec22b-P33 induced higher cytosolic calcium levels than GFP-Sec22b. Left: SOCE (200–400 s time interval) peak values presented as mean \pm s.e.m.; $n = 43$ GFP-Sec22b-expressing cells and $n = 32$ GFP-Sec22b-P33-expressing cells from 3 independent experiments; Student's t -test: $***P < 0.0005$; NS, not significant.

Sec22 interacts with lipid transfer proteins, and inhibition of Sec22 leads to defects in lipid metabolism at contact sites between ER and PM in yeast

Sites of close proximity between ER and PM have been extensively studied in yeast, where they were shown to play an important role in regulating PtdIns(4)P metabolism^{8,41} and cell growth⁴². Thus, we tested whether our findings in neurons would be conserved in yeast.

We confirmed that Sec22 is required for yeast growth (Supplementary Fig. 3a), and interacts with the yeast homologue of Stx1 (Sso1; Fig. 6a), but not during Sso1 transit through the secretory pathway (Fig. 6b,c,d). For non-vesicular lipid transfer to be efficient, cytosolic lipid transfer proteins concentrate at MCSs through interaction with components of the MCSs (refs 8,43,44). Hence, we tested whether our proposed *trans*-SNARE bridge interacted with lipid transfer proteins. Both Sso1 and

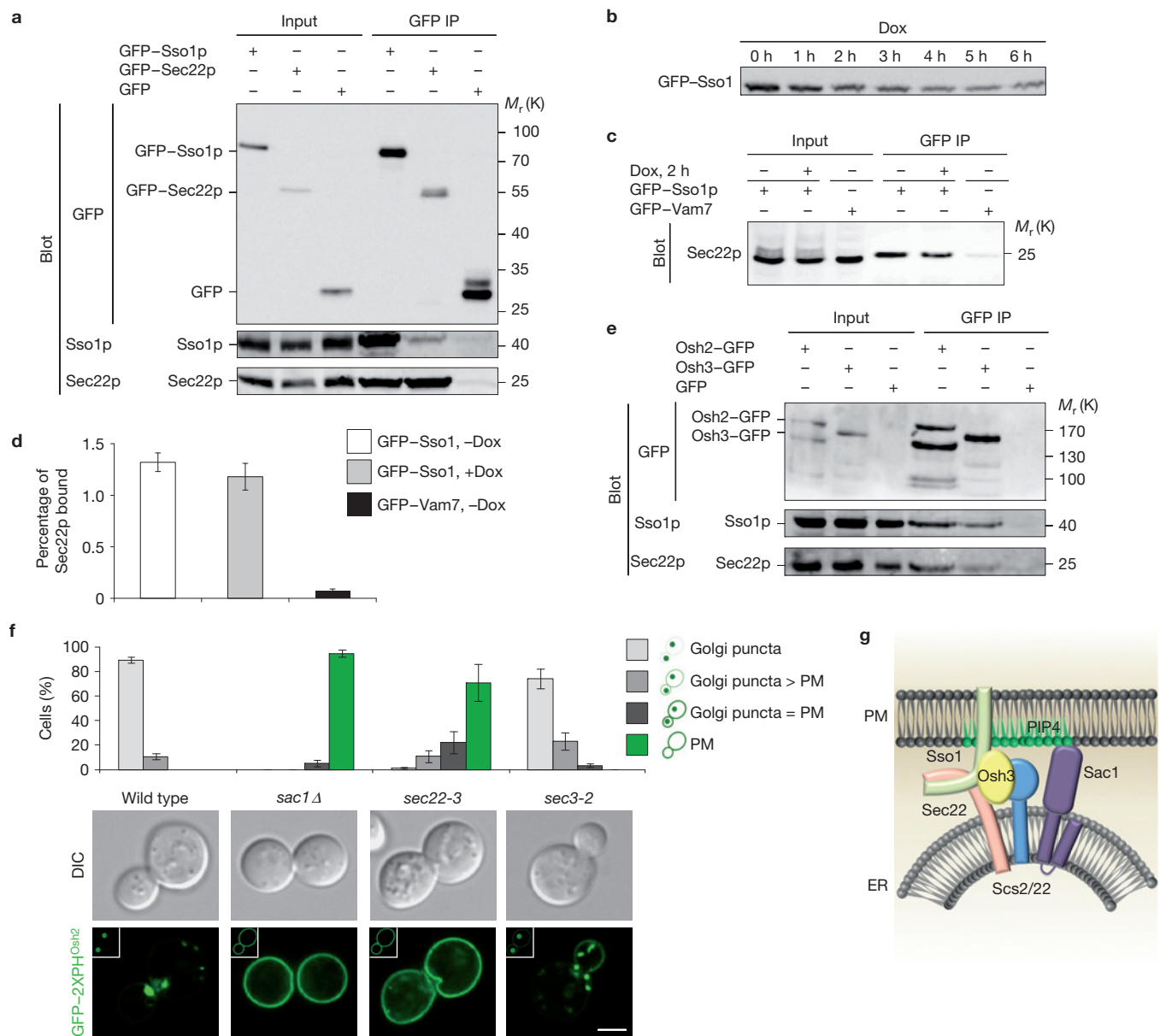


Figure 6 Sec22 interacts with lipid transfer proteins, and inhibition of Sec22 leads to defects in lipid metabolism at contact sites between ER and PM in yeast. **(a)** Sso1 and Sec22 interaction shown by co-immunoprecipitation. After crosslinking carried out in intact cells, lysates of wild-type BY4742 yeast expressing GFP-Sso1 or GFP-Sec22p were immunoprecipitated with GFP antibodies. We confirmed that GFP-Sso1 localized normally (Supplementary Fig. 3b). Total cell lysate (input) and immunoprecipitated fractions were subjected to western blotting using GFP (upper panel), Sso1 (middle panel) or Sec22 (lower panel) antibodies. Input lanes contained 3% of extract used for immunoprecipitations (Methods). **(b-d)** Sso1 and Sec22 do not interact during the time that Sso1 transits through the secretory pathway. **(b)** Wild-type cells (SEY6210) carrying a plasmid encoding GFP-Sso1 (pAP87-GFP-Sso1) under the control of a tetracycline-repressible promoter were grown overnight in normal growth medium to induce GFP-Sso1 expression, and then shifted to repression conditions by addition of $10 \mu\text{g ml}^{-1}$ doxycycline; cells were prepared for western analysis at the indicated time points, and immunoblotting was carried out using Sso1 antibodies. **(c)** Wild-type (SEY6210) cells carrying pAP87-GFP-Sso1 grown in normal growth medium with or without doxycycline for 2 h were subjected to immunoprecipitation analysis with GFP antibodies, and then blotted with Sec22 antibodies. Input

lanes contain 3% of material used for immunoprecipitations. **(d)** Mean and s.d. of $n=3$ independent experiments carried out as in **c** are shown. **(e)** Sec22 and Sso1 interact physically with the MCS lipid transfer proteins Osh2 and Osh3. Immunoprecipitations of BY4741 cells expressing Osh2-GFP, Osh3-GFP and wild-type cells expressing GFP alone were performed with GFP antibodies as described in **a**. Immunoblotting was carried out using Sso1 and Sec22 antibodies to reveal endogenous proteins. **(f)** The *sec22-3* ts mutant is defective in PtdIns(4)P metabolism at ER-PM contact sites. The indicated yeast strains expressing the PtdIns(4)P-specific probe GFP-2xPH^{Osh2} were incubated for 30 min at 37°C , and then imaged by confocal microscopy. Quantifications of GFP signal in cell populations, with the 4 scored patterns indicated in the legend, are shown in the upper panel. Representative images are shown in the lower panel. Mean and s.d. of 4 independent experiments are given ($n=307$ GFP-expressing cells for wild type, 341 for *sac1Δ*, 498 for *sec22-3* and 285 for *sec3-2*). Student's *t*-test for Golgi PtdIns(4)P pattern of wild type compared with *sec22-3* is $P < 0.001$. Scale bar: $3 \mu\text{m}$. **(g)** Model of Sso1-Sec22 interaction at yeast ER-PM contact sites. Schematic diagram of the ER-PM MCS components regulating PtdIns(4)P based on published data^{8,55} and our results. Uncropped images of blots are shown in Supplementary Fig. 5.

Sec22 co-immunoprecipitated with the lipid transfer proteins Osh2 and Osh3 (Fig. 6e), which are known to be enriched at ER–PM contact sites^{8,9} (Fig. 6g), where the PM level of PtdIns(4)P is regulated^{8,42}. Next, we evaluated the yeast temperature-sensitive (ts) Sec22 mutant *sec22-3*. We found an increased PM concentration of PtdIns(4)P in *sec22-3* grown at the non-permissive temperature (Fig. 6f), as previously shown for mutants of other components of the MCSs, namely Sac1 and Osh3 (ref. 38). The observed phenotype does not seem to be due to impaired secretion, as the *sec3-2* mutant defective in the late secretory pathway did not show a similar phenotype (Fig. 6f). Localization of Sac1 was not affected in *sec22-3* (Supplementary Fig. 3c). These results together strongly suggest contact site defects in *sec22-3* (Fig. 6f,g)⁸.

DISCUSSION

Together, our results support a role for Sec22-mediated ER–PM MCSs in non-vesicular lipid regulation and transfer, which could contribute to the function of Sec22b in neuronal PM expansion (Fig. 4l). Consistent with our findings, loss of MCSs in yeast was recently reported to impair growth⁴². MCSs are sites of active lipid synthesis⁹ and blocking vesicular trafficking was shown to have little effect on the transport of phospholipids, sterols and subsets of sphingolipids¹⁰. Hence, we favour the possibility of bulk non-vesicular lipid transfer from the ER to the PM contributing to cell surface growth. Non-vesicular lipid transfer at MCSs is thought to be involved in lipid modulation and signalling^{45,46}, which could contribute to neuronal growth by secondarily affecting the secretory pathway⁴⁷. In addition to lipid modulation, neuronal growth and guidance are modulated by intracellular calcium levels⁴⁸. Sec22b (this study) and ER–PM MCS-localized E-Syts (ref. 41) are not required for SOCE. As shown for E-Syts, our results suggest that Sec22b and STIM1–Orai1 represent independent ER–PM crosstalk systems. The fact that increasing the length of Sec22b (this study) strongly affects SOCE suggests that the dominant-negative effect on ER–PM minimal distance decreases the efficiency of SOCE. It is interesting to note that Sec22b and Stx1 interaction persists in the adult brain (Fig. 3b). Considering the extent of neuronal remodelling that occurs in the adults^{49,50} this suggests that the role of Sec22b in neurite growth unravelled here could extend to axonal and dendritic remodelling in adult brains. Furthermore, Sec22b could probably generate ER–PM SNARE bridges with other PM Q-SNAREs such as Stx2/3/4 because non-neuronal cells do not express Stx1 and the former are closely related molecules. Taking into account that both Sec22b and PM syntaxins also have well-described functions in the secretory pathway, Sec22b-mediated SNARE bridges could provide a direct balance between non-vesicular and vesicular transport^{51,52}. Future directions should address the precise structure, function and regulation of the Sec22b/syntaxin complex, and notably its role in coordinating vesicular traffic and non-vesicular processes to mediate PM expansion.

In conclusion, we are led to propose that the R-SNARE Sec22b and the PM Q-SNARE syntaxin form a *trans*-SNARE bridge that brings the ER and PM into close apposition without mediating their fusion. This close proximity may be particularly critical in conditions of massive growth of the PM such as during neurite extension, to minimize the inter-membrane distance, which in turn would maximize the efficiency of lipid synthesis and transfer^{53,54}. □

METHODS

Methods and any associated references are available in the [online version of the paper](#).

Note: Supplementary Information is available in the online version of the paper

ACKNOWLEDGEMENTS

We are grateful to F. Polleux, V. Medvedeva and A. Assali for advice on *in utero* electroporation, N. Rouach for calcium imaging and F. Perez for the gift of RUSH reagents. We are grateful to Y. N. Jan for support to M.P. in revising the manuscript, and L. Bosanac for support with software. We are grateful to A. Pierani and members of the Galli laboratory for discussions. We acknowledge France-BioImaging infrastructure supported by the French National Research Agency (ANR-10-INSB-04, 'Investments for the future'). Work in our group was financially supported in part by grants from INSERM, CNRS, the Association Française contre les Myopathies (AFM), the Association pour la Recherche sur le Cancer (ARC), the Mairie de Paris Medical Research and Health Program, the Fondation pour la Recherche Médicale (FRM), the Ecole des Neurosciences de Paris (ENP), and awards of the Association Robert Debré pour la Recherche Médicale to T.G., ANR JC grant to D.T. and the Ecole des Neurosciences de Paris (ENP) and award of the Fondation des Treilles to M.P. F.D. is supported by a PhD fellowship from Paris Descartes University and funds by the PhD Program Ecole Doctorale Frontières du Vivant (FdV)—Programme Bettencourt.

AUTHOR CONTRIBUTIONS

M.P., C.L.J. and T.G. conceived the project. M.P. generated and analysed data in mammalian cells and neurons, and A.J. in budding yeast. F.D. and D.T. performed and analysed liposome fusion assays. M.P., C.G.S. and I.I. performed and C.G.S. and I.I. analysed results from super-resolution microscopy; X.D. and A.T. set-up the super-resolution microscopes. M.P. and K.H.P. performed and analysed subcellular fractionation experiments. D.V. and J.-M.V. generated and analysed electron microscopy data. M.P., C.L.J. and T.G. wrote the manuscript.

COMPETING FINANCIAL INTERESTS

The authors declare no competing financial interests.

Published online at www.nature.com/doi/10.1038/ncb2937

Reprints and permissions information is available online at www.nature.com/reprints

- Hanus, C. & Ehlers, M. D. Secretory outposts for the local processing of membrane cargo in neuronal dendrites. *Traffic* **9**, 1437–1445 (2008).
- Pfenninger, K. H. Plasma membrane expansion: a neuron's Herculean task. *Nat. Rev. Neurosci.* **10**, 251–261 (2009).
- Futerman, A. H. & Banker, G. A. The economics of neurite outgrowth—the addition of new membrane to growing axons. *Trends Neurosci.* **19**, 144–149 (1996).
- Martinez-Arca, S., Alberts, P., Zahraoui, A., Louvard, D. & Galli, T. Role of tetanus neurotoxin insensitive vesicle-associated membrane protein (TI-VAMP) in vesicular transport mediating neurite outgrowth. *J. Cell Biol.* **149**, 889–900 (2000).
- Alberts, P. *et al.* Cross talk between tetanus neurotoxin-insensitive vesicle-associated membrane protein-mediated transport and L1-mediated adhesion. *Mol. Biol. Cell* **14**, 4207–4220 (2003).
- Gupton, S. L. & Gertler, F. B. Integrin signaling switches the cytoskeletal and exocytic machinery that drives neurite outgrowth. *Dev. Cell* **18**, 725–736 (2010).
- Schulte, C., Racchetti, G., D'Alessandro, R. & Meldolesi, J. A new form of neurite outgrowth sustained by the exocytosis of enlargosomes expressed under the control of REST. *Traffic* **11**, 1304–1314 (2010).
- Stefan, C. J. *et al.* Osh proteins regulate phosphoinositide metabolism at ER-plasma membrane contact sites. *Cell* **144**, 389–401 (2011).
- Tavassoli, S. *et al.* Plasma membrane–endoplasmic reticulum contact sites regulate phosphatidylcholine synthesis. *EMBO Rep.* **14**, 434–440 (2013).
- Voelker, D. R. Genetic and biochemical analysis of non-vesicular lipid traffic. *Annu. Rev. Biochem.* **78**, 827–856 (2009).
- Jahn, R. & Scheller, R. H. SNAREs—engines for membrane fusion. *Nat. Rev. Mol. Cell Biol.* **7**, 631–643 (2006).
- Gao, Y. *et al.* Single reconstituted neuronal SNARE complexes zipper in three distinct stages. *Science* **337**, 1340–1343 (2012).
- Hernandez, J. M. *et al.* Membrane fusion intermediates via directional and full assembly of the SNARE complex. *Science* **336**, 1581–1584 (2012).
- Martinez-Arca, S. *et al.* A common exocytic mechanism mediates axonal and dendritic outgrowth. *J. Neurosci.* **21**, 3830–3838 (2001).
- Danglot, L. *et al.* Role of TI-VAMP and CD82 in EGFR cell-surface dynamics and signaling. *J. Cell Sci.* **123**, 723–735 (2010).
- Schoch, S. *et al.* SNARE function analysed in synaptobrevin/VAMP knockout mice. *Science* **294**, 1117–1122 (2001).

17. Zylbersztein, K. *et al.* The vesicular SNARE synaptobrevin is required for semaphorin 3A axonal repulsion. *J. Cell Biol.* **196**, 37–46 (2012).
18. Pfenninger, K. H. Transport and insertion of membrane components into processes of growing neurons. *Neurosci. Res. Prog. Bull.* **20**, 73–79 (1981).
19. Lockerbie, R. O., Miller, V. E. & Pfenninger, K. H. Regulated plasmalemmal expansion in nerve growth cones. *J. Cell Biol.* **112**, 1215–1227 (1991).
20. Liu, Y. T., Flanagan, J. J. & Barlowe, C. Sec22p export from the endoplasmic reticulum is independent of SNARE pairing. *J. Biol. Chem.* **279**, 27225–27232 (2004).
21. Burgo, A. *et al.* A molecular network for the transport of the TI-VAMP/VAMP7 vesicles from cell center to periphery. *Dev. Cell* **23**, 166–180 (2012).
22. Burgo, A. *et al.* Role of Varp, a Rab21 exchange factor and TI-VAMP/VAMP7 partner, in neurite growth. *EMBO Rep.* **10**, 1117–1124 (2009).
23. Rossi, V. *et al.* Longins and their longin domains: regulated SNAREs and multifunctional SNARE regulators. *Trends Biochem. Sci.* **29**, 682–688 (2004).
24. Chaîneau, M., Danglot, L. & Galli, T. Multiple roles of the vesicular-SNARE TI-VAMP in post-Golgi and endosomal trafficking. *FEBS Lett.* **583**, 3817–3826 (2009).
25. Mancias, J. D. & Goldberg, J. The transport signal on Sec22 for packaging into COPII-coated vesicles is a conformational epitope. *Mol. Cell* **26**, 403–414 (2007).
26. Cebrian, I. *et al.* Sec22b regulates phagosomal maturation and antigen cross-presentation by dendritic cells. *Cell* **147**, 1355–1368 (2011).
27. Xu, D., Joglekar, A. P., Williams, A. L. & Hay, J. C. Subunit structure of a mammalian ER/Golgi SNARE complex. *J. Biol. Chem.* **275**, 39631–39639 (2000).
28. Martínez-Arca, S. *et al.* A dual mechanism controlling the localization and function of exocytic v-SNAREs. *Proc. Natl Acad. Sci. USA* **100**, 9011–9016 (2003).
29. Becher, A., Drenckhahn, A., Pahnner, I. & Ahnert-Hilger, G. The synaptophysin-synaptobrevin complex is developmentally upregulated in cultivated neurons but is absent in neuroendocrine cells. *Eur. J. Cell Biol.* **78**, 650–656 (1999).
30. Lang, T. *et al.* SNAREs are concentrated in cholesterol-dependent clusters that define docking and fusion sites for exocytosis. *EMBO J.* **20**, 2202–2213 (2001).
31. Touret, N. *et al.* Quantitative and dynamic assessment of the contribution of the ER to phagosome formation. *Cell* **123**, 157–170 (2005).
32. Izeddin, I. *et al.* Super-resolution dynamic imaging of dendritic spines using a low-affinity photoconvertible actin probe. *PLoS ONE* **6**, e15611 (2011).
33. Specht, C. G. *et al.* Quantitative nanoscopy of inhibitory synapses: counting gephyrin molecules and receptor binding sites. *Neuron* **79**, 308–321 (2013).
34. Li, F. *et al.* Energetics and dynamics of SNAREpin folding across lipid bilayers. *Nat. Struct. Mol. Biol.* **14**, 890–896 (2007).
35. Arora, P. S., Ansari, A. Z., Best, T. P., Ptashne, M. & Dervan, P. B. Design of artificial transcriptional activators with rigid poly-L-proline linkers. *J. Am. Chem. Soc.* **124**, 13067–13071 (2002).
36. Boncompain, G. *et al.* Synchronization of secretory protein traffic in populations of cells. *Nat. Methods* **9**, 493–498 (2012).
37. Hogan, P. G., Lewis, R. S. & Rao, A. Molecular basis of calcium signaling in lymphocytes: STIM and ORAI. *Annu. Rev. Immunol.* **28**, 491–533 (2010).
38. Cahalan, M. D. STIMulating store-operated Ca²⁺ entry. *Nat. Cell Biol.* **11**, 669–677 (2009).
39. Palmer, A. E., Jin, C., Reed, J. C. & Tsien, R. Y. Bcl-2-mediated alterations in endoplasmic reticulum Ca²⁺ analyzed with an improved genetically encoded fluorescent sensor. *Proc. Natl Acad. Sci. USA* **101**, 17404–17409 (2004).
40. Miao, Y. *et al.* An essential and NSF independent role for alpha-SNAP in store-operated calcium entry. *eLife* **2**, e00802 (2013).
41. Giordano, F. *et al.* PI(4,5)P(2)-dependent and Ca²⁺-regulated ER-PM interactions mediated by the extended synaptotagmins. *Cell* **153**, 1494–1509 (2013).
42. Manford, A. G., Stefan, C. J., Yuan, H. L., Macgurn, J. A. & Emr, S. D. ER-to-plasma membrane tethering proteins regulate cell signaling and ER morphology. *Dev. Cell* **23**, 1129–1140 (2012).
43. Peretti, D., Dahan, N., Shimoni, E., Hirschberg, K. & Lev, S. Coordinated lipid transfer between the endoplasmic reticulum and the Golgi complex requires the VAP proteins and is essential for Golgi-mediated transport. *Mol. Biol. Cell* **19**, 3871–3884 (2008).
44. Amarilio, R., Ramachandran, S., Sabanay, H. & Lev, S. Differential regulation of endoplasmic reticulum structure through VAP-Nir protein interaction. *J. Biol. Chem.* **280**, 5934–5944 (2005).
45. Boss, W. F. & Im, Y. J. Phosphoinositide signaling. *Annu. Rev. Plant Biol.* **63**, 409–429 (2012).
46. Andersen, O. S. & Koepp, R. E. 2nd Bilayer thickness and membrane protein function: an energetic perspective. *Annu. Rev. Biophys. Biomol. Struct.* **36**, 107–130 (2007).
47. Domanska, M. K., Kiessling, V. & Tamm, L. K. Docking and fast fusion of synaptobrevin vesicles depends on the lipid compositions of the vesicle and the acceptor SNARE complex-containing target membrane. *Biophys. J.* **99**, 2936–2946 (2010).
48. Henley, J. & Poo, M. M. Guiding neuronal growth cones using Ca²⁺ signals. *Trends Cell Biol.* **14**, 320–330 (2004).
49. Chen, J. L. *et al.* Structural basis for the role of inhibition in facilitating adult brain plasticity. *Nat. Neurosci.* **14**, 587–594 (2011).
50. Lee, W. C. *et al.* Dynamic remodeling of dendritic arbors in GABAergic interneurons of adult visual cortex. *PLoS Biol.* **4**, e29 (2006).
51. Zhang, D., Vjestica, A. & Oliferenko, S. Plasma membrane tethering of the cortical ER necessitates its finely reticulated architecture. *Curr. Biol.* **22**, 2048–2052 (2012).
52. D'Angelo, G. *et al.* Vesicular and non-vesicular transport feed distinct glycosylation pathways in the Golgi. *Nature* **501**, 116–120 (2013).
53. Levine, T. & Rabouille, C. Endoplasmic reticulum: one continuous network compartmentalized by extrinsic cues. *Curr. Opin. Cell Biol.* **17**, 362–368 (2005).
54. Prinz, W. A. Lipid trafficking sans vesicles: where, why, how?. *Cell* **143**, 870–874 (2010).
55. De Saint-Jean, M. *et al.* Osh4p exchanges sterols for phosphatidylinositol 4-phosphate between lipid bilayers. *J. Cell Biol.* **195**, 965–978 (2011).

METHODS

Plasmids and antibodies. The plasmids used in this study are listed in Supplementary Table 1. Sec22b cDNA (pQE9-ERS24) was a gift from F. Paumet (Thomas Jefferson University, USA). mEos2 and Dendra2 cDNA were gifts from X. Darzacq (IBENS, France). pCAG-EGFP was a gift from F. Polleux (The Scripps Research Institute, USA). PtdIns(4)P FLARE GFP-2xPH^{oh2} was a gift from C. Stefan and S. Emr (Cornell University, USA), and pGK27 GFP-Sac1 a gift from P. Mayinger (Oregon Health & Science University, USA). pAc-GFP-Sec61 β and pEGFP-C1 were purchased from Addgene (Plasmid 15108), and Clontech, respectively. Plasmids pAP87-GFP-Sso1 and pCM188-GFP-Sec22 have been described previously⁶⁰.

Polyclonal antibody against nucleoporins mAb414 (1:100) was a gift from V. Doye (Institut Jacques Monod, France). Anti-VAMP2/Syb2 (monoclonal antibody Cl69.1, 1:1,000) and SNAP-25 (mAb Cl71.1, 1:1,000) were gifts from R. Jahn (MPI-Göttingen, Germany). Anti-syntaxin1 (monoclonal antibody HPC-1, 1:1,000) was a gift from C. Barnstable (Yale University, USA). Sso1 (rabbit polyclonal serum, 1:10,000), and Sec22 (rabbit polyclonal, purified 1:1,000) antibodies were gifts from J. Jantti (University of Helsinki, Finland), and H. D. Schmitt (MPI for Biophysical Chemistry, Germany) respectively. We used interchangeably 3 different antibodies against mouse Sec22b with no observable difference: ERS24 antibody (1:1,000) was received as a gift from J. E. Rothman (Yale University, USA) and commercial antibodies were purchased from Synaptic Systems (Cat. No 186003, 1:1,000) and Proteintech (Cat. No 14776-1-AP, 1:1,000). Antibodies against SNAP-23 (1:500), VAMP4 (1:500) and TI-VAMP/VAMP7 (1:500) were previously described^{56–58}. All other antibodies against calreticulin (ThermoScientific, Cat. No PA3-900, 1:1,000), ERGIC53 (monoclonal antibody G1/93, Enzo Life Sciences, Cat. No ALX-804-602-C100 1:1,000), synapsins (Cat. No 106 003, 1:500) and Ykt6 (Synaptic Systems, 1:500), VGlut1 (Millipore, Cat. No AB5905, 1:1,000), tubulin (Hybridoma Bank, Cat. No E7, 1:2,000), GFP (monoclonal antibody clones 7.1 and 13.1, Cat. No 11814460001, 1:1,000) and Tau (Cat. No 1289977, 1:1,000) (Roche Diagnostics), MAP2 (Abcam, Cat. No ab5392, 1:10,000) and GAP-43 (Millipore, Cat. No AB5220, 1:1,000) were commercially available.

siRNAs for Sec22b knockdown in culture were obtained from Qiagen (Cat. No SI01413097; SI01413083). Previously validated shRNA vectors for Sec22b knockdown *in vivo*⁵⁹ were obtained from Sigma (Cat. No NM_011342; NM_011342).

Chemicals. The lipids used in this study—1,2-dioleoyl-*sn*-glycero-3-phosphocholine (PC), 1,2-dioleoyl-*sn*-glycero-3-phosphoethanolamine (PE), 1,2-dioleoyl-*sn*-glycero-3-phospho-L-serine (PS), 1,2-dioleoyl-*sn*-glycero-3-phosphoethanolamine-*N*-(lissamine rhodamine B sulphonyl) (PE-RHO) and 1,2-dioleoyl-*sn*-glycero-3-phosphoethanolamine-*N*-(7-nitro-2-1,3-benzoxadiazol-4-yl) (PE-NBD)—were purchased from Avanti Polar Lipids as chloroform solutions.

Yeast strains and growth conditions. *Saccharomyces cerevisiae* strains SEY6210 *MAT α ura3-52 leu2-3,112 his3- Δ 200 lys2-801 trp1- Δ 901 suc2- Δ 9*, DBY2056 *MAT α ura3-52, RSY279 MAT α his4-619 ura3-52 sec22-3*, NY412 *MAT α ura3-52 sec3-2*, BY4742 *sac1 Δ MAT α his3 Δ 1 leu2 Δ 0 lys2 Δ 0 ura3 Δ 0 sac1 Δ :kanMX*, BY4741 *Osh2-GFP MAT α his3 Δ 1 leu2 Δ 0 lys2 Δ 0 ura3 Δ 0 Osh2::GFPkanMX6* and BY4741 *Osh3-GFP MAT α his3 Δ 1 leu2 Δ 0 lys2 Δ 0 ura3 Δ 0 Osh3::GFPkanMX6* were used in this study. Yeast media used, growth assays carried out, Tet promoter plasmids pAP87 and pCM188, and induction conditions were as described previously⁶⁰.

Yeast two-hybrid analysis. The coding sequence for amino acids 1–196 of human Sec22b was PCR-amplified and cloned into pB29 as an N-terminal fusion to LexA. The construct was verified by sequencing the entire insert and used as bait by Hybrigenics Services (www.hybrigenics-services.com) to screen a highly complex human fetal brain domain library constructed in pP6. pB29 and pP6 derive from the original pBTM116 (ref. 61) and pGADGH plasmids, respectively. One hundred and sixteen million clones (11-fold the complexity of the library) were screened using a mating approach with Y187 (*MAT α*) and L40 Δ Gal4 (*MAT α*) yeast strains as previously described⁶². Sixteen His⁺ colonies were selected on a medium lacking tryptophan, leucine and histidine. The prey fragments of the positive clones were amplified by PCR and sequenced at their 5' and 3' junctions. The resulting sequences were used to identify the corresponding interacting proteins in the GenBank database (NCBI) using a fully automated procedure.

Growth cone membrane subcellular fractionation. Growth cone membranes were prepared as described previously^{63–65}. Briefly, whole brains from newborn mice were homogenized in 0.32 M sucrose containing 1 mM MgCl₂, 2 mM TES buffer (pH 7.3), and Roche EDTA-free cocktail of protein inhibitors. Low-speed (Beckman rotor SW55 TI, 853g, 7 min) supernatant (LSS) of the homogenate was layered onto 0.83 M sucrose containing 1 mM MgCl₂, 2 mM TES buffer (pH 7.3), and Roche EDTA-free cocktail of protein inhibitors, and spun to equilibrium at

287,000g for 54 min in the SW55 TI rotor (Beckman). The GCP fraction at the 0.32/0.83 M-sucrose interface was collected, diluted with 0.32 sucrose solution and spun at 25,000 r.p.m. for 20 min in the SW55 TI rotor. The pellet was resuspended in lysis buffer (6 mM Tris-HCl, pH 8.01, 0.5 mM EDTA). Low-speed (SW55 TI, 3,000 rpm, 10 min) supernatant was spun in a TLAI20.2 rotor (Beckman) for 18 min at 76,000 r.p.m. Growth cone membranes were collected in the pellet. During the procedure, samples were collected: H, total brain homogenate; LSP, low-speed pellet; LSS, low-speed supernatant; GCP, the parent fraction of growth cone particles; A, fraction A (which contains soluble proteins of the homogenate and growth cone particles); B, fraction B (which contains the pellet after gradient centrifugation); mGCP, growth cone membranes. The success of every subcellular fractionation performed was evaluated by specific enrichment of GAP, a marker of axonal growth cones. Quantitative data were obtained by fluorescence western blot analysis of proteins of interest where the ratio of the signal intensity in growth cone membranes (mGCP) versus total brain homogenate (H) fractions was measured in a minimum of 3 independent fractionation experiments and expressed as means \pm s.e.m. GAP43 and nucleoporins are measured as positive and negative controls, respectively.

Protein expression and purification. Mammalian SNARE proteins were expressed in *Escherichia coli* and purified using His-tag affinity purification. All SNARE proteins used in this study (Sec22b-His₆, co-expressed Δ Habc-Stx1/His₆-SNAP25, Δ Habc-Stx1-His₆ and His₆-SNAP25) were expressed in the BL21(DE3) *Escherichia coli* bacterial strain and purified by nickel affinity chromatography essentially as described previously⁶⁶. Briefly, a 6 l culture in Luria Broth (LB) medium was grown at 37 °C to an attenuation of 0.7 (at 600 nm) and was then induced with 1 mM isopropyl- β -D-thiogalacto-pyranoside (IPTG) for 3 h at 37 °C. The cells were collected by centrifugation and re-suspended in 50 ml of breaking buffer (25 mM HEPES/KOH (pH 7.5), 150 mM KCl, 10% (w/v) glycerol, 1 mM dithiothreitol and 1% (w/v) Triton X-100) with 2 mini-tablets of EDTA-free protease inhibitors. The cells were broken by sonication. After ultra-centrifugation of the lysate, the supernatant was incubated with 3 ml of Ni-NTA beads (Merck) for 2 h at 4 °C. The beads were rinsed with washing buffer (25 mM HEPES/KOH (pH 7.5), 150 mM KCl, 10% (w/v) glycerol, 1 mM dithiothreitol and 1% (w/v) octyl- β -D-glucopyranoside) and the protein was eluted with a step gradient from 100 to 500 mM imidazole.

Proteoliposome reconstitution. The R-SNARE protein was reconstituted with the donor lipid mix mimicking the ER membrane lipid composition^{67,68}: 68 mol% PC, 3 mol% cholesterol, 25 mol% PE, 1 mol% PS, 1.5 mol% PE-RHO and 1.5 mol% PE-NBD. The Q-SNARE protein was reconstituted with the acceptor lipid mix mimicking the PM lipid composition⁶⁸: 35 mol% PC, 30 mol% cholesterol, 25 mol% PE and 10 mol% PS. SNARE proteins were incorporated into liposomes using the standard method^{69,70}. The appropriate lipid mixture (0.9 μ mol; in chloroform) was dried in a glass tube for 10 min under a gentle stream of nitrogen, and for 1 h under vacuum. The dried lipid film was resuspended in 300 μ l of SNARE proteins diluted at the appropriate concentration in buffer A (25 mM HEPES/KOH (pH 7.5), 150 mM KCl, 1 mM dithiothreitol, 10% (v/v) glycerol and 1% (w/v) octyl- β -D-glucopyranoside), under vigorous vortexing for 1 h at room temperature. The detergent concentration was next reduced to 0.33% (w/v) by rapid dilution in buffer B (25 mM HEPES/KOH (pH 7.5), 150 mM KCl, 1 mM dithiothreitol and 10% (v/v) glycerol), and then removed by overnight flow dialysis against 4 l of buffer B. Proteoliposomes were isolated on a Nycodenz flotation gradient as previously described⁵⁹ and preserved on ice for up to 2 weeks. Sec22b R-SNARE liposomes and various Q-SNARE liposomes (co-expressed Q-SNARE: Stx1A/SNAP25 protein; separately expressed Q-SNARE: Stx1A+SNAP25 formed following incubation of Stx1A liposomes with the SNAP25 protein; and Stx1 protein) were generated and reconstituted at a \sim 1:400 protein/lipid molar ratio.

SNARE-mediated lipid-mixing assay. Twenty-two microlitres of Q-SNARE liposomes (\sim 0.44 mM of lipids final) was added to 96-well FluoroNunc plates (Fisher Scientific) and pre-warmed at 37 °C for 5 min. The fusion reaction was initiated by adding 3 μ l of R-SNARE liposomes (\sim 0.06 mM of lipids final) and 25 μ l of buffer B at room temperature. Fusion between Q- and R-SNARE liposomes was measured by following the dequenching of the PE-NBD fluorescence resulting from its dilution into the fused liposomes⁶⁹. The NBD fluorescence was monitored at 2-min intervals for 120 min (excitation at 485 nm; emission at 535 nm) by the Wallac 1420 Victor (Perkin Elmer) plate reader equilibrated to 37 °C. After 120 min, 10 μ l of 2.5% (w/v) *n*-dodecylmaltoside was added to completely dissolve the liposomes and thus measure the NBD fluorescence at infinite dilution; the data were then normalized as previously described⁶⁹.

Immunoprecipitation. Mouse brains or transfected COS7 cells were lysed in lysis buffer (50 mM HEPES at pH 7.2, 100 mM NaCl, 4 mM EGTA and 2 mM

MgCl₂) at 4 °C. After 30 min of centrifugation at 13,000 r.p.m. with a Beckman table centrifuge, total proteins were quantified with Bradford assays. Two milligrams of total proteins at 1 mg ml⁻¹ total protein concentration was incubated overnight at 4 °C with 10 µg of antibody crosslinked to 300 µg of protein G Dynabeads (Applied Biosystems) and prewashed with lysis buffer. As the expected band for Sec22b in western blots is at the size of mouse immunoglobulin light chains, antibodies were crosslinked to the protein G Dynabeads. Additionally, all Sec22b antibodies used were generated in rabbit. After removal of supernatant and three washes of the beads with the lysis buffer, proteins were eluted with 50 mM glycine at pH 2.5. Eluted proteins were denatured and loaded on 4–12% BisTris NuPAGE gel (Applied Biosystems). Input (25 µg or 50 µg) was loaded on gels, as well as the eluate of the immunoprecipitate with the specific antibody and the immunoprecipitate with the corresponding IgG negative control. The gels were transferred to a nitrocellulose membrane for western blot staining. The membranes were blocked for 30 min, cut when appropriate to allow for blotting with multiple antibodies of proteins with a similar molecular weight and incubated with primary antibody in TBS with 1% Tween-20 and 5% milk overnight at 4 °C. After three washes, fluorescent secondary antibodies were incubated for 2 h at room temperature in 1% Tween-20 in TBS, and signals were visualized with the fluorescent antibodies on the Odyssey system (LI-COR Biosciences) that allows for quantitative analysis of the signal intensity.

For immunoprecipitations from budding yeast using *in vivo* crosslinking, cells were grown to D_{600} between 0.5 and 1 in selective medium at 24 °C, collected by centrifugation, washed once with 100 mM Tris-HCl, at pH 9.4, and 10 mM dithiothreitol, resuspended to 100 D_{600} units of cells ml⁻¹ in the same buffer and incubated for 15 min at 24 °C with gentle agitation. Cells were collected by centrifugation and resuspended in 1 M sorbitol and 20 mM PIPES, at pH 6.8 at 20 D_{600} units ml⁻¹. 40 units of zymolyase 100T (MP Biomedicals) were added, cells were incubated with gentle shaking for 30 min at 30 °C, and then spheroplasts were collected by centrifugation and resuspended in the same buffer at a concentration of 5 D_{600} units ml⁻¹. DSP (dithiobis succinimidylpropionate) (Pierce) crosslinker was added to a final concentration of 200 µg ml⁻¹, followed by incubation at room temperature for 30 min at 80 r.p.m. Quenching was performed for 15 min by addition of 0.1 M Tris-HCl (pH 8.0). Spheroplasts were hypotonically lysed in 20 mM PIPES, pH 6.8, 200 mM sorbitol, 5 mM MgCl₂, 1 mM phenylmethylsulphonyl fluoride and protease inhibitor cocktail (Roche). Immunoprecipitations were performed using purified GFP binding protein⁷¹ (GBP) bound covalently to AminoLink resin, according to the manufacturer's instructions (Thermo Scientific Pierce), after pre-clearing with AminoLink resin alone. After elution in SDS sample buffer, β-mercaptoethanol was added for 30 min at 37 °C for reverse crosslinking. One per cent of total extract (input) and 33% of immunoprecipitated fractions were loaded onto gels developed with Sso1 and Sec22 antibodies; 1% total extract and 12% of immunoprecipitated fractions for GFP blots. After transfer, membranes were cut when appropriate to allow for blotting with multiple primary antibodies, and then were visualized with horseradish peroxidase-conjugated secondary antibodies.

Neuronal culture and in utero electroporation. All experiments involving mice were performed in accordance with the directive 2010/63/EU of the European Parliament and of the Council of 22 September 2010 on the protection of animals used for scientific purposes and approved by the CEEA40-Comité d'éthique Buffon. We used *Mus musculus* Swiss strain timed-pregnant females to obtain embryos at gestation days E14.5 and E15, and newborn P0 mice as indicated in the results and/or legends and Supplementary Information. All efforts were taken to minimize the number of animals, and we estimate to have used 50 timed-pregnant females for this study and resulting progeny.

Neuronal cultures were performed using E15 embryos from timed-pregnant Swiss mice. Cortical neurons were dissected and dissociated before being plated in loading medium (MEM, fetal calf serum, glutamine and glucose) on glass coverslips precoated with poly-L-lysine and laminin (100 µg ml⁻¹ each) or only poly-L-lysine. After 2 h of attachment, culture medium was changed to Neurobasal medium supplemented with B27 and glutamine. Neurons were transfected at DIV1 with GFP or GFP-Sec22b, and fixed and analysed after 24 h of expression; neurons transfected with scrambled+GFP, siRNA1+GFP and siRNA+GFP-Sec22b were fixed and analysed after 48 h of expression (see Supplementary Section 14). Neurons were transfected with GFP-Sec22b, GFP-Sec22b-P10, GFP-Sec22b-P20 and GFP-Sec22b-P33 at DIV1 and fixed and analysed after 16 h of expression.

In utero electroporation was performed as previously described⁷². Endotoxin-free shRNA or scrambled DNA was co-injected with EGFP under the CAG promoter in equimolar quantities at a concentration of 1 µg µl⁻¹ in the lateral ventricles. We used timed-pregnant Swiss females and performed in utero electroporation at E14.5 followed by short-term survival until E17.5. The electroporation settings were as follows: 5 pulses of 45 V for 50 ms with 900 ms intervals. In utero electroporation surgeries for three conditions (scrambled+CAG-GFP,

shRNA1+CAG-GFP, shRNA2+CAG-GFP) were done on the same day in a random order. Two independent sets of surgeries were performed, with two to three timed-pregnant female mice per condition in each set of surgeries. The investigators were not blinded to allocation during surgery and retrieval of GFP-positive embryonic brains. The investigators were blinded in the subsequent experimental steps: cutting the GFP-positive embryonic brains, imaging of brain sections, quantification and data analysis. Blinding was performed by assigning random labels to GFP-positive brains by a colleague.

Immunohistochemistry and immunochemistry. Cortical neuron cultures were fixed for 15 min with 4% PFA; quenched for 30 min in autofluorescence reducing solution (50 mM NH₄Cl in PBS); permeabilized for 4 min with 0.1% Triton X-100 in PBS; and blocked for 30 min in 0.25% fish gelatin in PBS. Primary antibodies were incubated overnight at 4 °C in 0.125% fish gelatin in PBS. After 3 washes, secondary antibodies were incubated for 45 min at room temperature before mounting in Prolong medium (Applied Biosystems).

Embryonic brains at E17.5 were retrieved and fixed with 4% PFA overnight at 4 °C. Following fixation, brains were washed in PBS and embedded in 3% low melting agarose. Coronal brain sections (100 µm) were obtained using a vibrating microtome (Leica VT1200S). Sections were processed for immunostaining by incubation for 20 min in autofluorescence reducing solution (50 mM NH₄Cl in PBS), followed by blocking solution (0.25% gelatin and 0.1X Triton in PBS) for 3 h. Primary antibody was incubated in diluted blocking solution (0.125% gelatin and 0.1X Triton in PBS) overnight at 4 °C, followed by three washes in PBS and incubation in secondary antibodies (Molecular probes) diluted in blocking solution for 3 h at room temperature. Excess secondary antibody was removed by washing three times in PBS and slices were mounted on slides using Vectashield mounting medium.

Surface staining. Cortical neurons and HeLa cells were surface labelled in the following manner: Neurobasal medium was replaced with ice-cold DMEM with 20 mM HEPES containing primary antibody. Cells were incubated for 5–10 min on ice. Cells were washed with ice-cold DMEM with 20 mM HEPES and PBS to remove unbound antibody, and fixed with 4% PFA for 10 min on ice followed by 10 min at room temperature. Cells were permeabilized and the total pool of tagged proteins was detected with different primary antibodies, followed by detection with the corresponding secondary antibodies. Images were acquired on an epifluorescence microscope (Supplementary Section 15) with the same exposure in all conditions, and measured using MetaMorph. Presence at the PM was expressed as the ratio between total and surface signal. Statistical significance was evaluated using GraphPad Prism.

RUSH secretory assay. The RUSH secretory assay was performed as previously published³⁶. Briefly, HeLa cells were co-transfected with GFP-Sec22b or GFP-Sec22b-P33 and mCherry-tagged VSV-G RUSH construct. HeLa cells were plated in biotin-free medium blocking VSV-G in the ER. Exit from the ER of VSV-G was obtained by addition of biotin, and cells were fixed 30 min, 60 min and 6 h after biotin addition to the medium as indicated. The amount of surface VSV-G was evaluated by surface staining and expressed as the ratio to total VSV-G, and normalized to the negative control, which were cells not treated with biotin ($t = 0$ min). Obtained data were analysed for statistical significance with Student's *t*-test.

Morphometric analysis. To measure neurite length, neurons in culture were imaged with an epifluorescence microscope where per neuron axonal length and the length of the three longest dendrites was measured (Supplementary Section 15). To measure neurite length of neurons in brain sections following *in utero* electroporation, z-stack was acquired. Brain sections with similar targeting of the electroporation in the same coronal plane were used for all analysis. Length of the leading edge of GFP-positive electroporated neurons was evaluated on maximal intensity projection generated in ImageJ. Neurite length was measured in Metamorph.

Analysis of distribution of GFP-positive cells in subdivisions of cortex was done on confocal images using ImageJ. The subdivisions were determined on the basis of DAPI staining and transferred to threshold images of the GFP signal, where the number of GFP-positive neurons was measured with the Analyse particle tool in ImageJ, using the same parameters for all images.

Statistical significance was evaluated using GraphPad Prism.

Molecular biology. PCRs for construction were performed using Phusion polymerase, according to the manufacturer's instructions. Primers and linkers were bought from Sigma-Aldrich. A description of all constructs designed for this study is given in Supplementary Table 1.

Cortical neurons in culture were transfected with Lipofectamine2000 according to the manufacturer's instructions. COS7 cells were either transfected with Lipofectamine2,000 for live imaging, or electroporated as previously described¹⁴.

HeLa cells were transfected with X-tremeGENE DNA for RUSH secretory assay. HeLa cells were co-transfected according to the manufacturer's instruction with Lipofectamine2,000 co-transfecting scrambled or siRNA1 with D1ER, and they were imaged after 48 h of expression.

Conventional microscopy. Neurons, COS7 and HeLa cells were imaged using an inverted epifluorescence microscope (DMI6000B; Leica) or a confocal microscope (Zeiss 710). Three-dimensional reconstruction was done on the acquired confocal *z*-stack using Imaris software. Yeast cells were imaged using an inverted microscope (DM IRE2; Leica) equipped with a 10-MHz CCD (charge-coupled device) camera (CoolSNAP_{HQ}; Roper Scientific) using a $\times 100$ NA 1.40 objective. Deconvolution of confocal *z*-series was performed using Metamorph software.

Super-resolution microscopy. Super-resolution PALM and STORM imaging was performed as described previously^{32,33}. Briefly, for single-colour PALM experiments, cortical neurons transfected at DIV1 with pCMV-mEOS2-Sec22b and fixed with 4% PFA at DIV2 were imaged in PBS, using a 405 nm laser for photoconversion and a 561 nm laser for imaging. Dual-colour STORM/PALM experiments (2D and 3D) were performed on cortical neurons transfected at DIV1 with Stx1-pHluorin and mEOS2-Sec22b or Sec22b-Dendra2, and surface stained at DIV2 with anti-GFP to reveal PM Stx1, followed by fixation with 4% PFA and immunostaining with Alexa 647-coupled secondary antibody. Only Stx1-pHluorin localized at the PM was surface-labelled with anti-GFP and Alexa 647-tagged secondary antibodies and visualized by STORM imaging. mEOS2-Sec22b or Sec22b-Dendra2 were imaged by PALM. We used Dendra2 instead of mEOS2 for C-terminal tagging of Sec22b, as mEOS2 seems not to fold properly when expressed in the lumen of the ER (unpublished observation).

Two-dimensional super-resolution data were acquired on an inverted Nikon Ti Eclipse microscope, equipped with an external laser platform (405 nm, 532 nm, 561 nm, 639 nm) for PALM and dSTORM³². Imaging was done sequentially in reducing buffer (PBS, pH 7.4, containing 10% glucose, 50 mM β -mercaptoethylamine, 0.5 mg ml⁻¹ glucose oxidase and 40 μ g ml⁻¹ catalase, degassed with N₂), by first acquiring single Alexa 647 signals using a 532 nm and a 639 nm laser (STORM), followed by the acquisition of mEOS2 or Dendra2 signals (405 nm and 561 nm lasers; PALM). On average 20,000 frames were collected per image in 2D super-resolution, and 40,000 per image in 3D super-resolution experiments. For 2D imaging, the fluorophore detections were fitted with a 2D Gaussian distribution using an adapted version of the MTT algorithm and were x/y -drift corrected with the positions of multicoloured beads (TetraSpeck, Invitrogen, 100 nm diameter) that had been immobilized on the coverslip as fiducial markers. Super-resolution image reconstructions were rendered with a 2D Gaussian distribution with a standard deviation $\sigma = 10$ nm and with a pixel size of 10 nm (for detail see ref. 32).

The 3D experiments were carried out on a separate imaging set-up with the same overall specifications⁷³, but equipped with an adaptive optics system MicAO (Imagine Optic) that served to correct for aberrations of the point spread function and to induce astigmatism. Inducing a controlled astigmatic deformation (amplitude 0.06 μ m) to the single fluorophore detections was done to retrieve their *z*-axis positions with nanometric resolution, as described recently³³. Calibration curves for the *z*-axis position were made from 3D image stacks of 100 nm beads taken at a step size of 24 nm in both fluorescence channels (593 nm and 684 nm emission).

The goal of the super-resolution analysis was to determine minimal distance between Sec22b and PM Stx1. The 2D projection and 3D Euclidean distances between co-localizing Sec22b and surface syntaxin1 molecules were measured in the same 3D acquisitions by calculating the vectorial distance between the centres of mass of the multiple detections in each channel. Given the stochastic nature of single-molecule imaging, only those Sec22b detections that were in close proximity to surface syntaxin detections (within 100 nm in 2D projections and within 250 nm in 3D) were considered in the quantification.

For representation of the 3D super-resolution images, we used the ViSP visualization tool⁷⁴.

Calcium imaging. We measured cytosolic calcium with the cell-permeable dye Fura2, and ER luminal calcium with the ER-localized FRET-based ratiometric Ca²⁺-sensor D1ER. HeLa cells transfected with GFP-Sec22b or GFP-Sec22b-P33 were loaded with Fura2 for 30 min at room temperature in calcium (1 mM Ca) imaging buffer with Pluronic acid at 1:500 dilution and Fura2 at 2 μ M. Cells were washed with calcium imaging buffer (1 mM Ca²⁺) to remove Fura2 from the medium and left for an additional 15 min at room temperature, followed by a wash with calcium-free imaging buffer in which the cells were incubated for 30 min. Imaging was done on an epifluorescence microscope (see Supplementary Section 15) with a GFP band-pass filter to localize transfected cells before the imaging, and set-up with filters and an ultraviolet lamp suitable for excitation at 340 nm and 380 nm, and emission at 510 nm. Imaging was done with acquisition every 5 s for 600 s. CPA was added

at 100 s at a final concentration 20 μ M, calcium solution at a final concentration 2 mM at 200 s, and ionomycin at 400 s at a final concentration 10 μ M. Cells were analysed with ImageJ software. HeLa cells were co-transfected with D1ER, and either mCherry constructs (mCherry, mCherry-Sec22b or mCherry-Sec22P33) or Sec22b siRNA. Cells were depleted of extracellular calcium for 30 min in calcium-free imaging buffer, followed by time-lapse imaging. Imaging was done on a Zeiss710 confocal microscope, with excitation at 405 nm and emission measured for EGFP at 441–510 nm and EYFP at 513–561 nm. Images were acquired every 5 s for 900 s. Calcium at a final concentration of 2 mM was added at 150 s. Ionomycin at a final concentration of 10 μ M was added at 640 s. Acquired time-lapse images were analysed with ImageJ software. The response to calcium addition was fitted with a single exponential ($f(x) = a + (b - a) * (1 - \exp^{-cx})$) using GraphPad Prism and the difference between the rates in three conditions was statistically evaluated with nonlinear regression analysis. Peak values of calcium entry (150–640 s time interval) were presented as mean \pm s.e.m.

Electron tomography. For electron tomography, cultured cells expressing either GFP-Sec22b or GFP-Sec22b-P33 constructs were fixed with 1% glutaraldehyde, post-fixed in 2% osmium ferrocyanide for 1 h, washed 5 \times 3 min in H₂O, followed by 1% thiocarbonylhydrazide for 20 min, washed, further incubated for 30 min in 2% OsO₄, washed and incubated overnight in 1% uranyl acetate. The next day, the cells were washed and incubated in lead aspartate for 30 min and washed again. The samples were then dehydrated in graded ethanol solutions, infiltrated and embedded in Durcupan resin (Electron Microscopy Sciences). Sections (300 nm thick) were cut, and collected on Formvar-coated copper slot electron microscopy grids. The grids were stained in 2% uranyl acetate in 70% methanol for 10 min, washed and stained for another 10 min in 1% lead citrate. Before imaging, the grids were labelled on both sides with 15 nm gold particles used as fiducials markers. Double-tilt tomography stacks were acquired in a 300 kV Tecnai F30 microscope (FEI) equipped with a 2k US100 camera (Gatan), using SerialEM acquisition software⁷⁵. The pixel size of tilt series was 2.5 nm. Tomograms were reconstructed from the tilt series with the IMOD software⁷⁶.

ER-PM contact sites were identified visually on electron tomograms in IMOD. Membrane spacing (the distance between adjacent membranes) was measured on single views with the IMOD modeller. Multiple contact sites were measured for each condition, and for each contact site, multiple measurements were made along the region of contact and averaged.

Yeast PtdIns(4)P assay. Strains transformed with pRS416-GFP-2xPH^{Sh2} were grown to mid-logarithmic phase in selective medium, then transferred to rich YPD medium for 3–4 h before imaging, with or without a shift of temperature to 37 °C for 30 min, and cells were maintained at the growth temperature during imaging. For each condition, 250–500 GFP-expressing cells from 4 independent experiments were scored for 1 of 4 GFP patterns, and then the mean and standard deviation were calculated. The 4 GFP patterns scored were: primarily Golgi puncta; strong Golgi puncta, weak PM; equivalent Golgi puncta and PM signals; and primarily PM.

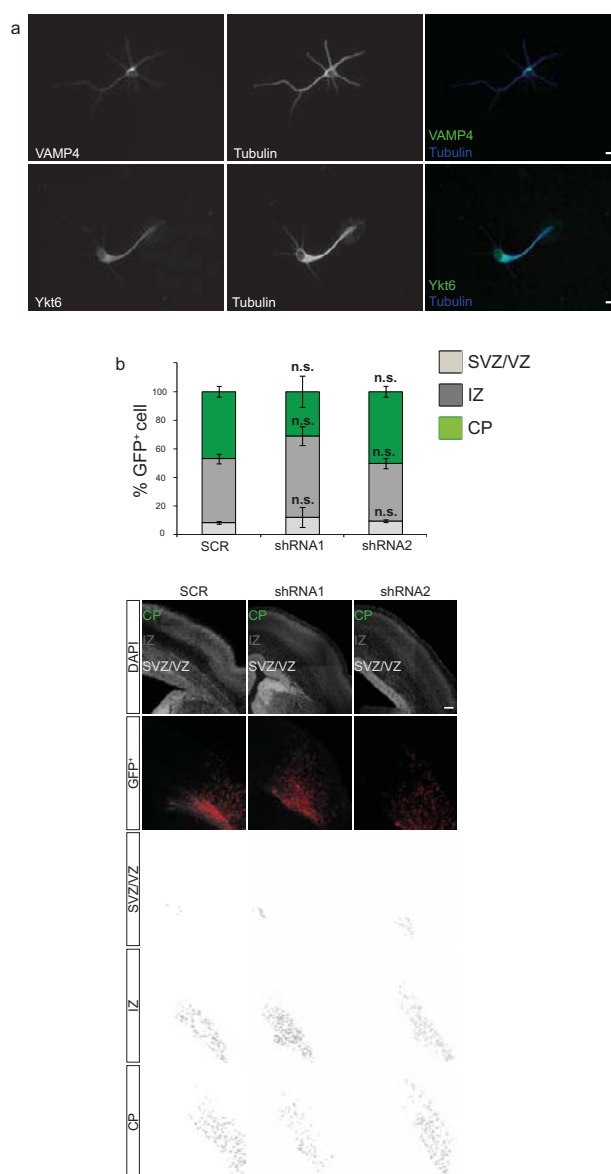
Statistics. We used Student's *t*-test or one-way ANOVA with post-tests Dunnett or Bonferroni-corrected *t*-test. The calcium curves were analysed with nonlinear regression analysis after fitting with a single exponential function ($f(x) = a + (b - a) * (1 - \exp^{-cx})$). Electron microscopy data comparing distance at MCSs between cells transfected with wild-type and mutant Sec22b were analysed with the Kolmogorov-Smirnov test. The Kolmogorov-Smirnov test was also used to evaluate distance measurements between EOS-Sec22b and Sec22b-Dendra2 to the PM Stx1, as revealed by super-resolution PALM/STORM.

No statistical method was used to determine sample size in any of the experiments.

56. Galli, T. *et al.* A novel tetanus neurotoxin-insensitive vesicle-associated membrane protein in SNARE complexes of the apical plasma membrane of epithelial cells. *Mol. Biol. Cell* **9**, 1437–1448 (1998).
57. Mallard, F. *et al.* Early/recycling endosomes-to-TGN transport involves two SNARE complexes and a Rab6 isoform. *J. Cell Biol.* **156**, 653–664 (2002).
58. Muzerelle, A. *et al.* Tetanus neurotoxin-insensitive vesicle-associated membrane protein localizes to a presynaptic membrane compartment in selected terminal subsets of the rat brain. *Neurosci.* **122**, 59–75 (2003).
59. Cebrian, I. *et al.* Sec22b regulates phagosomal maturation and antigen crosspresentation by dendritic cells. *Cell* **147**, 1355–1368 (2011).
60. Pranke, I. M. *et al.* α -Synuclein and ALPS motifs are membrane curvature sensors whose contrasting chemistry mediates selective vesicle binding. *J. Cell Biol.* **194**, 89–103 (2011).
61. Vojtek, A. B. & Hollenberg, S. M. Ras-Raf interaction: two-hybrid analysis. *Methods Enzymol.* **255**, 331–342 (1995).
62. Fromont-Racine, M., Rain, J. C. & Legrain, P. Toward a functional analysis of the yeast genome through exhaustive two-hybrid screens. *Nat. Genet.* **16**, 277–282 (1997).

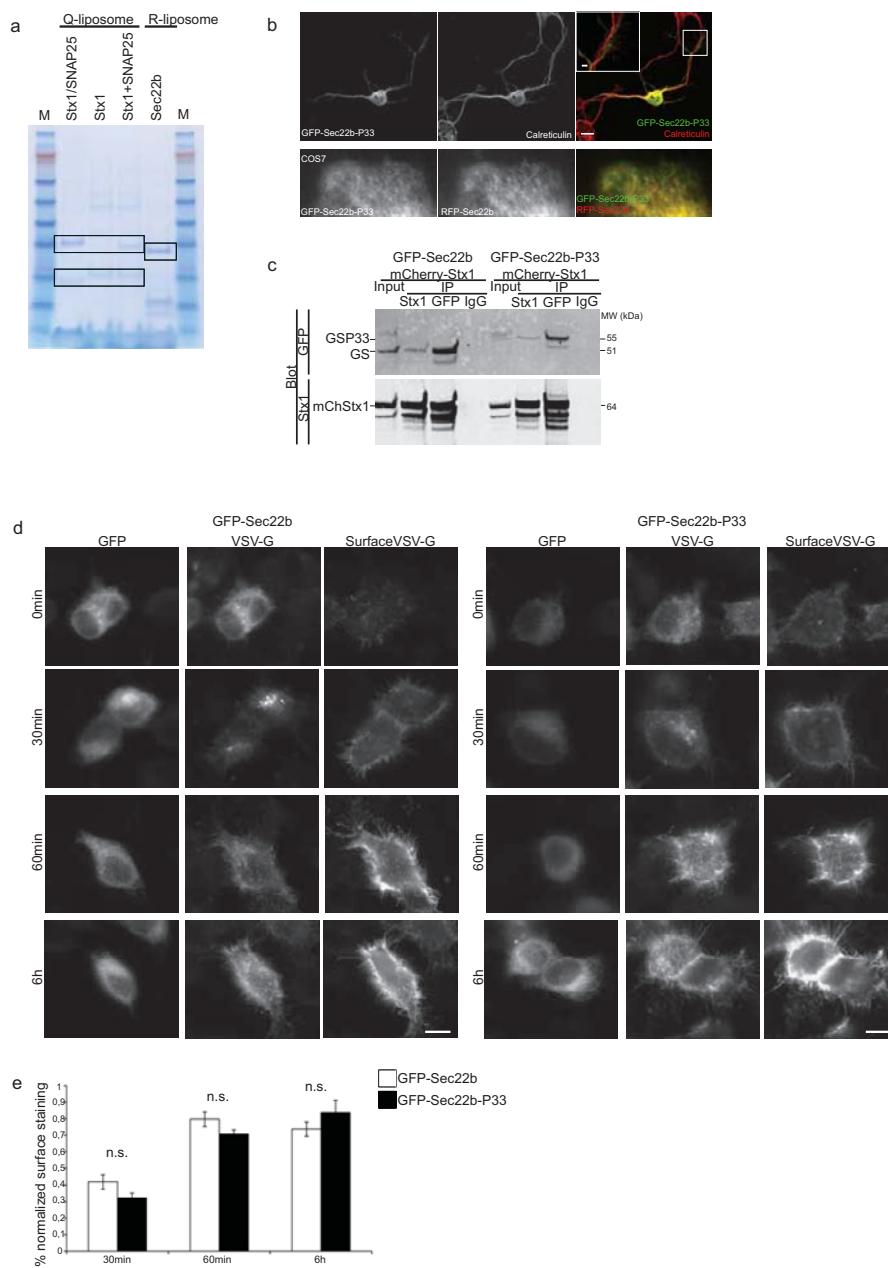
63. Lohse, K. *et al.* Axonal origin and purity of growth cones isolated from fetal rat brain. *Brain Res. Dev. Brain Res.* **96**, 83–96 (1996).
64. Pfenninger, K. H., Ellis, L., Johnson, M. P., Friedman, L. B. & Somlo, S. Nerve growth cones isolated from fetal rat brain: subcellular fractionation and characterization. *Cell* **35**, 573–584 (1983).
65. Ellis, L., Katz, F. & Pfenninger, K. H. Nerve growth cones isolated from fetal rat brain. II. Cyclic adenosine 3':5'-monophosphate (cAMP)-binding proteins and cAMP-dependent protein phosphorylation. *J. Neurosci.* **5**, 1393–1401 (1985).
66. Tareste, D., Shen, J., Melia, T. J. & Rothman, J. E. SNAREpin/Munc18 promotes adhesion and fusion of large vesicles to giant membranes. *Proc. Natl Acad. Sci. USA* **105**, 2380–2385 (2008).
67. Swift, L. L. Assembly of very low density lipoproteins in rat liver: a study of nascent particles recovered from the rough endoplasmic reticulum. *J. Lipid Res.* **36**, 395–406 (1995).
68. Van Meer, G. & de Kroon, A. I. Lipid map of the mammalian cell. *J. Cell Sci.* **124**, 5–8 (2011).
69. Weber, T. *et al.* SNAREpins: minimal machinery for membrane fusion. *Cell* **92**, 759–772 (1998).
70. Ji, H. *et al.* Protein determinants of SNARE-mediated lipid mixing. *Biophys. J.* **99**, 553–560 (2010).
71. Rothbauer, U. *et al.* A versatile nanotrapp for biochemical and functional studies with fluorescent fusion proteins. *Mol. Cell. Proteom.* **7**, 282–289 (2008).
72. Saito, T. *In vivo* electroporation in the embryonic mouse central nervous system. *Nat. Protocols* **1**, 1552–1558 (2006).
73. Izeddin, I. *et al.* Wavelet analysis for single molecule localization microscopy. *Opt. Express* **20**, 2081–2095 (2012).
74. El Beheiry, M. & Dahan, M. ViSP: representing single-particle localizations in three dimensions. *Nat. Methods* **10**, 689–690 (2013).
75. Mastronarde, D. N. Automated electron microscope tomography using robust prediction of specimen movements. *J. Struct. Biol.* **152**, 36–51 (2005).
76. Kremer, J. R., Mastronarde, D. N. & McIntosh, J. R. Computer visualization of three-dimensional image data using IMOD. *J. Struct. Biol.* **116**, 71–76 (1996).

DOI: 10.1038/ncb2937



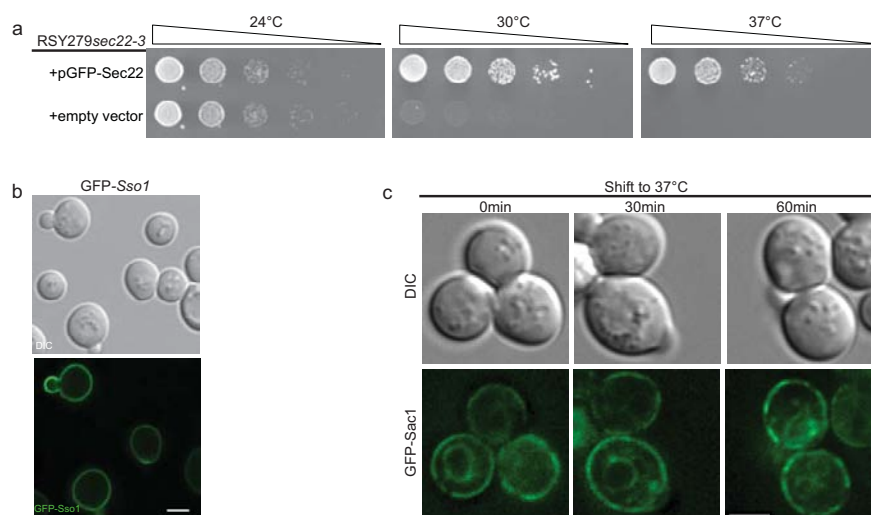
Supplementary Figure 1 a. Immunocytochemistry of VAMP4 and Ykt6 in mouse cortical neurons, further showing observed strong growth cone enrichment is not a general characteristic of R-SNAREs, but specific to a subset of them (Sec22b, VAMP2 and TI-VAMP). VAMP4 is abundant in the perikaryon, but sparsely present in the neurites, while Ykt6 is clearly detectable in neurites as well as perikaryon, but does not have strong localization in the growth cones. Scale bar 10 μ m. **b.** Impact of Sec22b knockdown *in vivo* on the distribution of neurons between subdivisions of cortex. *In utero* electroporation in wild type mouse brains was performed with shRNA1, shRNA2 or scrambled construct as control (scrambled: n=13 brain sections from 3 embryos; shRNA1: n=3 brain sections from 2 embryos; shRNA2: n=9 brain sections

from 3 embryos), co-electroporated with GFP under CAG promoter. **Lower panel:** Brain sections with similar targeting of the electroporation in the same coronal plane were subdivided into regions based on DAPI staining: cortical plate (CP), IZ (intermediate zone) and SVZ/VZ (subventricular/ventricular zone) (first row). Selected regions were transferred to threshold images of the GFP signal (second row), where GFP-positive neurons were outlined (third to fifth row) and measured with Analyze particle tool in ImageJ, using the same parameters for all images. **Upper panel:** GFP+ positive cells in each subdivision were expressed as percentage of total number of GFP+ cells \pm S.E.M. One way Anova showed no significant difference between conditions for all three regions. $P \geq 0.5$ n.s. non-significant. Scale bar 100 μ m.



Supplementary Figure 2 a. SDS-PAGE gel of R-SNARE (Sec22b) and Q-SNARE (co-expressed Stx1/SNAP25, separately expressed Stx1+SNAP25 or Stx1 alone) liposomes used in the lipid mixing assay (Fig.3g,h). Separately expressed Q-SNARE was formed by incubating Stx1 liposomes overnight on ice with SNAP25 in a 1:3 (Stx1:SNAP25) molar ratio followed by isolation on a Nycodenz flotation gradient. The smaller size of Stx1 in the case of co-expressed Q-SNAREs is due to the absence of His₆-tag. Lipids can be seen at the bottom of the gel. **b. Upper row:** Immunolocalization of GFP-Sec22b with a 33 proline linker and calreticulin antibody in cortical neurons. Scale bar: 10 μm, inset: 2 μm. **Lower row:** COS7 cells co-transfected with GFP-Sec22b containing 33 proline linker and RFP-Sec22b. **c.** Immunoprecipitation of GFP-Sec22b with 33 proline linker. COS7 cells were transfected with mCherry-Stx1 and GFP-Sec22b or the GFP-Sec22b with 33 proline linker. Immunoprecipitation was performed with mouse Stx1 antibody, mouse GFP antibody or mouse immunoglobulins as negative

control of specificity of immunoprecipitation. Western blot was revealed with rabbit GFP and syntaxin 1 antibodies. mCherry-Stx1 co-immunoprecipitated both GFP-Sec22b variants and *vice versa*. **d.,e.** RUSH secretory assay. HeLa cells were co-transfected with GFP-Sec22b or GFP-Sec22bP33 and mCherry tagged VSV-G RUSH construct blocked in the ER. Secretion is released with addition of biotin, and cells are fixed after 30min (n=76 cells for WT; n=96 cells for P33), 60min (n=92 for WT; n=99 for P33) and 6h (n=72 for WT; n=71 for P33). Amount of surface VSV-G was evaluated by surface staining and expressed as ratio to total VSV-G, and normalized to the negative control (n=77 for WT; n=72 for P33), which are cells never exposed to biotin (t=0min). **d.** Representative images are presented, with scale bar 10 μm. **e.** Mean value per condition and time point are shown, where error bars represent the S.E.M. Student t-test did not reveal any significant difference between the WT and P33 Sec22b constructs at any of the time points measured. P≥0,05 n.s.



Supplementary Figure 3 a. Growth defect of the temperature sensitive *sec22-3* yeast strain is rescued by expression of GFP-Sec22p. RSY279 *sec22-3* cells expressing GFP-Sec22 from a low-copy centromeric plasmid (pCM188-GFP-Sec22) were serially diluted onto medium selective for the plasmid and grown at 24°C (permissive) and at 30°C and 37°C (restrictive temperatures) for 2 days. **b.** Correct PM localization of GFP-Sso1 in wild type yeast cells. BY4742 GFP-Sso1 expressing cells in exponential

growth were imaged by confocal microscopy at 24°C; similar results were obtained for wild type cells (SEY6210). Scale bar 3 μ m. **c.** Sac1 (the PI4P phosphatase acting on the PM PI4P pool) is correctly localized in *sec22-3*. RSY279 *sec22-3* cells expressing GFP-Sac1 were incubated for 0, 30 or 60 minutes at 37°C, then imaged; representative images show normal ER localization of Sac1 at both time points after shift to restrictive temperature.

Fig. 1a

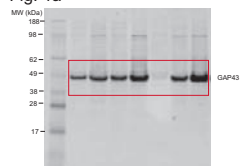


Fig. 1b

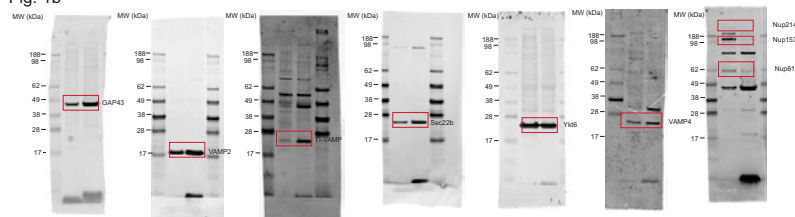


Fig. 3b

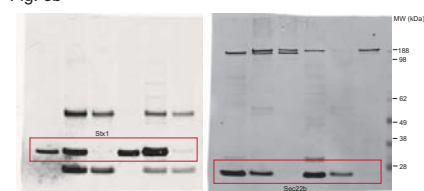


Fig. 3c

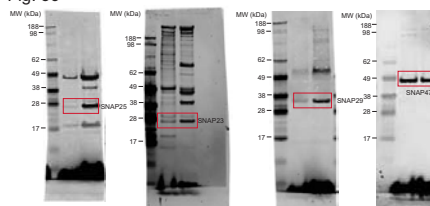


Fig. 3d

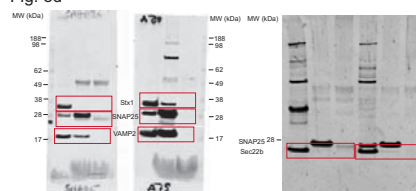


Fig. 3e

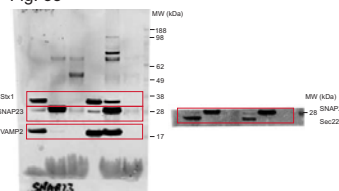
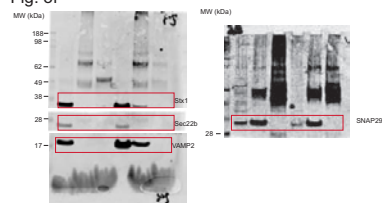
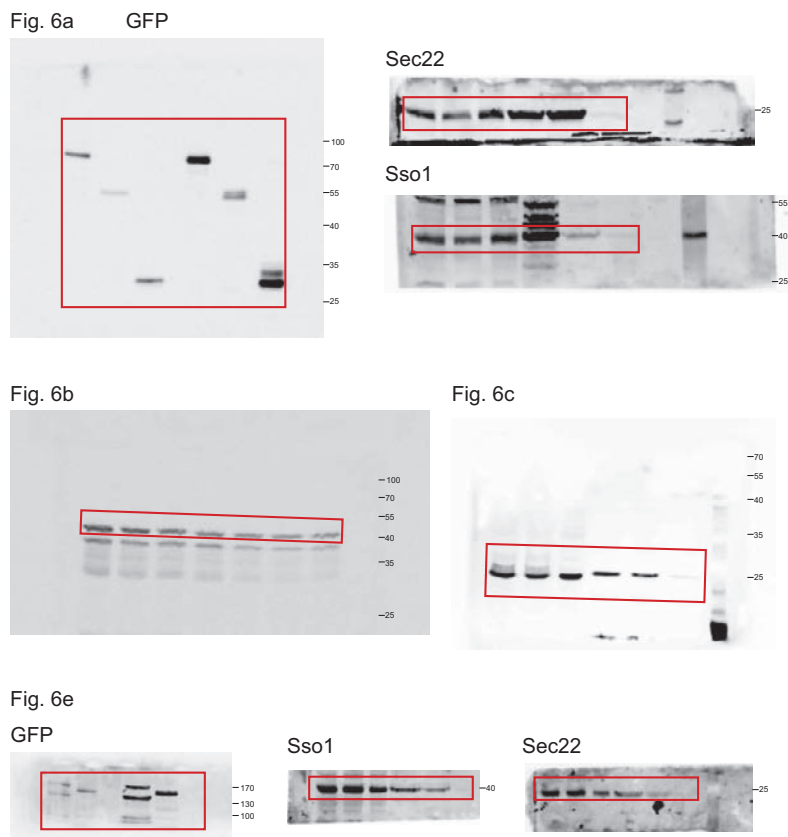


Fig. 3f



Supplementary Figure Western blots 1. Uncropped Western blots referring to main figures 1.a, 1.b, 3.b-f. Regions shown in main figures are marked with red squares. All Western blots were named according to the main figure to which they relate to. **Fig.1.a** Distribution analysis of growth cone fractionation showing specific enrichment of GAP43, axonal growth cone marker. **Fig.1.b** Enrichment of R-SNAREs in growth cone membrane fraction compared to total brain homogenate. GAP43 and nucleoporins were used as positive and negative control, respectively. **Fig.3.b** Western blot showing Stx1 immunoprecipitation from embryonic and adult brain, blotted for Stx1 on the left, and reblotted on the same membrane for Sec22b on the right. **Fig.3.c** Enrichment of SNAREs in growth cone membrane

fraction compared to total brain homogenate. **Fig.3.d** Western blot showing SNAP25 immunoprecipitation from embryonic and adult brain, blotted for SNAP25 and VAMP2, and Sec22b. Membrane on the left shows SNAP25 and VAMP2, and membrane on the right from a separate gel done in the same way shows SNAP-25 and Sec22b. **Fig.3.e** Western blot showing SNAP23 immunoprecipitation from embryonic and adult brain, blotted for SNAP23 and VAMP2 on the left, and reblotted on the same membrane for Sec22b on the right. **Fig.3.f** Western blot showing SNAP29 immunoprecipitation from embryonic and adult brain, blotted for Stx1, Sec 22b and VAMP2 on the left, and membrane on the right from a separate gel done in the same way shows SNAP-29.



Supplementary Figure Western blots 2. Uncropped Western blots referring to main figures 6.a-c, 6.e. Regions shown in main figures are marked with red squares. All Western blots were named according to the main figure to which they relate for simplicity. **Fig.6.a** Western blot showing GFP-Sso1 and GFP-Sec22p immunoprecipitation from yeast, blotted for GFP, Sso1 and Sec22p. **Fig.6.b** Western blot showing GFP-Sso1 expression over time

from plasmid under tetracycline-repressible promoter (pAP87-GFP-Sso1) stimulated with doxycycline. Membrane is blotted for Sec22. **Fig.6.c.** Western blot showing GFP immunoprecipitation from GFP-Sso1 and GFP-Vam7 expressing yeast cells, blotted for Sec22. **Fig.6.e** Western blot showing GFP immunoprecipitation from GFP-Osh2 and GFP-Osh3 expressing yeast cells, blotted for GFP, Sso1 and Sec22p.

Supplementary video files

Supplementary Video 1 Sec22b colocalizes with ER marker in COS7 cells. Videomicroscopy of COS7 cells co-transfected with mCherry-Sec22b and GFP-Sec61b reveals colocalization of the two constructs and clear ER morphology of the Sec22b compartment. Addition to **Fig.1g**.

Supplementary Video 2 Sec22b compartment has tubule-reticular morphology in neurites. Videomicroscopy of DIV2 mouse cortical neurons transfected with EGFP-Sec22b reveals clear tubulo-reticular morphology of the Sec22b compartment. Addition to **Fig.1g**.

Supplementary Video 3 Sec22b tubules enter growth cone filopodia. Confocal microscopy of DIV2 mouse cortical neurons transfected with EGFP-Sec22b reveals active dynamic of Sec22b tubules. Addition to **Fig.1g**

Supplementary Table

Supplementary Table 1. List of all the plasmids used in the study, the source of the plasmids, and if constructed for this study, details of the cloning procedure used to generate the construct.